An Optimal Atmospheric Circulation Mode in the Arctic Favoring Strong Summertime Sea Ice Melting and Ice-Albedo Feedback

IAN BAXTER^{a,b} AND OINGHUA DING^{a,b}

Department of Geography, University of California, Santa Barbara, Santa Barbara, California
 Earth Research Institute, University of California, Santa Barbara, Santa Barbara, California

(Manuscript received 31 August 2021, in final form 14 June 2022)

ABSTRACT: The rapid decline of summer Arctic sea ice over the past few decades has been driven by a combination of increasing greenhouse gases and internal variability of the climate system. However, uncertainties remain regarding spatial and temporal characteristics of the optimal internal atmospheric mode that most favors summer sea ice melting on low-frequency time scales. To pinpoint this mode, we conduct a suite of simulations in which atmospheric circulation is constrained by nudging tropospheric Arctic (60°-90°N) winds within the Community Earth System Model, version 1 (CESM1), to those from reanalysis. Each reanalysis year is repeated for over 10 model years using fixed greenhouse gas concentrations and the same initial conditions. Composites show the strongest September sea ice losses are closely preceded by a common June-August (JJA) barotropic anticyclonic circulation in the Arctic favoring shortwave absorption at the surface. Successive years of strong wind-driven melting also enhance declines in Arctic sea ice through enhancement of the ice-albedo feedback, reaching a quasi-equilibrium response after repeated wind forcing for over 5-6 years, as the effectiveness of the wind-driven ice-albedo feedback becomes saturated. Strong melting favored by a similar wind pattern as observations is detected in a long preindustrial simulation and 400-yr paleoclimate reanalysis, suggesting that a summer barotropic anticyclonic wind pattern represents the optimal internal atmospheric mode maximizing sea ice melting in both the model and natural world over a range of time scales. Considering strong contributions of this mode to changes in Arctic climate, a better understanding of its origin and maintenance is vital to improving future projections of Arctic sea ice.

KEYWORDS: Arctic; Sea ice; Data assimilation; Numerical analysis/modeling; Internal variability; Wind effects

1. Introduction

The rapid decline of Arctic sea ice, seen in all months over the last four decades, has become one of the most prominent symbols of a warming world. Most climate models predict this warming will lead to the first occurrence of ice-free summers in the Arctic sometime in the 2030s-2040s in response to the rise of anthropogenic greenhouse gases in the atmosphere (Overland and Wang 2013; Liu et al. 2013; Jahn et al. 2016; Jahn 2018; Screen and Deser 2019; Sigmond et al. 2018; Notz and SIMIP Community 2020; Bonan et al. 2021a; Diebold and Rudebusch 2021; Wang et al. 2021). However, the range of when an ice-free Arctic Ocean will likely occur and the rate of decline in sea ice cover is heavily influenced by lowfrequency variability of the climate system (Kay et al. 2011; Winton 2011; Notz and Marotzke 2012; Wettstein and Deser 2014; Zhang 2015; Swart et al. 2015; England et al. 2019; Bonan et al. 2021b) that is believed to be partially driven by natural SST variability in the tropics and extratropics (Screen and Deser 2019; Baxter et al. 2019; Bonan and Blanchard-Wrigglesworth 2020). Studies attempting to understand the extent of this contribution have suggested that internal variability may have accounted for 30%-50% of Arctic sea ice

Corresponding author: Ian Baxter, itbaxter@ucsb.edu

decline over the past 40 years (Stroeve et al. 2007; Kay et al. 2011; Stroeve et al. 2012; Zhang 2015; Ding et al. 2019; England et al. 2019) through impacts on large-scale atmospheric and oceanic processes in and around the Arctic. Oceanic processes associated with wind-driven gyre circulations and import of warm, salty water from lower latitudes has been linked to Arctic sea ice changes on decadal time scales (Lindsay and Zhang 2005; Polyakov et al. 2020). However, internally driven wind changes may only require several years to exert a melting impact on sea ice through atmospheric processes. Atmospheric circulation may be able to melt a substantial amount of Arctic sea ice within only a few years, such as the 6-yr period from 2007 to 2012 and strongly modulate anthropogenic impacts over the same time periods (Baxter et al. 2019). However, it remains quantitatively unclear how much sea ice loss during 2007-12 is due to wind forcing.

During the melt season, sea ice loss is determined by changes in surface radiative fluxes and temperature over the sea ice in addition to mechanical breakup and export of ice out of the Arctic (Ding et al. 2019; Olonscheck et al. 2019; Papritz 2020). Statistical analysis of reanalysis products has shown persistent anticyclonic circulation over the Arctic during summer can induce adiabatic descent of air from the middle to upper troposphere that can warm the near-surface atmosphere, enhancing downward longwave radiative fluxes and melting sea ice (Baxter et al. 2019; Papritz 2020). This summertime anticyclonic circulation can also strongly influence cloud cover, altering downwelling radiation at the surface (Huang et al. 2021), as well as enhance export of ice

Supplemental information related to this paper is available at the Journals Online website: https://doi.org/10.1175/JCLI-D-21-0679.s1.

through the Fram Strait (Smedsrud et al. 2017; Spreen et al. 2020). It was found that air masses with anticyclonic circulation produced clear-sky conditions in their center and cloudy conditions at their edges, leading to a complex combination of downwelling radiative fluxes dispersed around the anticyclone on a broad range of time scales (Wernli and Papritz 2018; Huang et al. 2021).

Although progress has been made to improve our physical understanding of the processes by which atmospheric circulation influences sea ice, the limited predictability of these processes in climate models constrains robust forecasts of end of summer sea ice to around June at best (Bushuk et al. 2020). Though recent Arctic sea ice change is dominated by a longterm decreasing trend, strong interannual variability is seen in the sea ice record, especially in the past decade, illustrated by the dispersion of extreme events such as the low sea ice cover events in 2007, 2012, 2016, 2019, and 2020 and the sea ice maximum event in 1996. Most current models have limited skill in predicting these interannual changes beyond a few months lead time and may struggle more in the future if thinner ice becomes more sensitive to atmospheric chaotic variability (Holland and Stroeve 2011; Wang et al. 2013; Msadek et al. 2014). We do not know to what degree these limitations are a result of current models' inability to capture important internal atmospheric processes in the polar regions and whether these internal processes possess some large-scale features that we can focus on to overcome the limited predictability of sea ice forecasts.

Many well-known modes of climate variability have been linked to Arctic sea ice loss, including the Pacific decadal variability (PDV), interdecadal Pacific oscillation (IPO), Atlantic multidecadal variability (AMV), and North Atlantic Oscillation (NAO) (Ogi et al. 2003; Meehl et al. 2018; Baxter et al. 2019; Screen and Deser 2019). Although internal atmospheric variability has been long known to have impacts on sea ice in observations, it is still unclear whether there exists an optimal internal mode that favors the strongest sea ice decline in the Arctic and the key mechanism through which this mode regulates sea ice variability. This question cannot be fully answered by diagnostic studies of observed records since so many driving forces of sea ice are mixed together and the observed sea ice changes thus represent a combination of responses to forcing originating from different sources. To address these questions, we conduct a set of nudging simulations by specifying observed winds into a fully coupled model to assess the sensitivity of the sea ice response to different wind patterns. We believe this strategy is unique in that it may pave new ground and develop a new perspective for studying the Arctic sea ice response to internal climate variability in climate models.

2. Strategy, data, and methods

a. The rationale of our strategy and expected outcome

Because large-scale circulation variability is believed to be most representative of internal viability in the high latitudes (Deser et al. 2012; Shepherd 2014; Ding et al. 2017), a model's

response to these observed winds may help us detect the optimal circulation mode that can excite the most significant sea ice change in the model. Once these modes can be identified in our nudging runs, we will then conduct an examination of the radiative fluxes and contributions to thermodynamic and dynamic ice loss associated with this mode and a comparison with observations that may shed more light on the fundamental mechanism contributing to sea ice variability in reality and climate models. The simulated sea ice response to this optimal mode in the nudging runs may also aid us to better estimate the largest magnitude of sea ice melting that could be attributed to internal atmospheric variability and thus constrain the uncertainty in projecting the occurrence of the first ice-free summer in the Arctic under different future warming scenarios. One limitation of our nudging simulations is that reliable reanalysis winds with 6-h temporal resolution in the Arctic only covers the recent 40 years, which is likely too short to reflect a full spectrum of all possible internal variability due to winds and may also contain imprints of anthropogenic forcing. Therefore, diagnostic analysis is also performed on a long (1800-yr) preindustrial simulation and 400-yr paleoclimate proxy data assimilated reconstructions reaching back to the seventeenth century to search for a circulation pattern that is closely associated with the strongest sea ice melting and warming epochs in the Arctic prior to the influence of anthropogenic emissions. These approaches using three independent data sources may improve our understanding of the common features of the optimal mode across different products and the sensitivity of this type of mode to anthropogenic forcing.

b. Data

1) NSIDC SEA ICE AND ERA-INTERIM

We examine monthly sea ice concentrations derived from Goddard edited passive microwave retrievals that have been compiled by the National Snow and Ice Data Center (NSIDC; Cavalieri et al. 1996; Fetterer and Knowles 2004). Our analysis is based on comparisons between total sea ice area (SIA) from the NSIDC and model simulations. Total sea ice volume and average sea ice thickness show consistent changes to SIA; therefore, we focus on SIA for simplicity. Total SIA is defined as the summed total of the product of the grid element area and sea ice concentration (>15%) in each Arctic grid cell. Total September SIA is primarily used to represent the annual minimum and aggregation of the preceding melt season. For winds and other atmospheric variables, we use the European Centre for Medium-Range Weather Forecasts (ECMWF)'s ERA-Interim (ERA-I; Dee et al. 2011) product. The ERA-I product has been evaluated over the Arctic in the previous studies, including surface temperature, radiative fluxes, precipitation, wind speed, and cloud properties (Lindsay et al. 2014; Graham et al. 2019; Wang et al. 2019).

CESM1-LE AND LONG PREINDUSTRIAL CONTROL SIMULATION

As a comprehensive resource for studying climate change in the presence of internal climate variability, the Community Earth System Model Large Ensemble (CESM1-LE; Kay et al. 2015) is run with fully coupled atmosphere, ocean, land, and sea ice components from 1920 to 2100. We use the mean of the 40 ensemble members, simulated using the same model and external forcing but with small round-off level variations in their initial air temperature field, as representative of our best estimate of the anthropogenically forced changes in total September SIA. To quantify the range of internal variability in the same model, we use 1800 years of the preindustrial (1850) fully coupled simulation, that uses fixed greenhouse gases to simulate internal processes inherent to the CESM1. Both the CESM1-LE and preindustrial control simulations use a nominal 1° resolution in the atmosphere model. CESM1 has shown an ability to capture general features of Arctic temperature, humidity, clouds, radiation, and sea ice. Particularly, the CESM1 simulated seasonal cycle of Arctic sea ice extent and the spatial distribution of sea ice thickness matches well with observations in the late twentieth century (Labe et al. 2018; England et al. 2019).

3) EBAF SURFACE AND TOA RADIATIVE FLUXES

To compare the radiative flux response to nudged winds in the CESM1 experiments we compare with the monthly and $1^{\circ} \times 1^{\circ}$ spatial resolution CERES EBAF-Surface Edition 4.1 radiative fluxes (EBAF). EBAF surface fluxes were calculated using the Langley modified Fu–Liou radiative transfer model with inputs from MODIS retrieved cloud properties, adjusted CERES outgoing TOA fluxes, meteorological data from NASA GMAO reanalysis, and aerosol data from an aerosol assimilation system. EBAF fluxes have been considered as a key benchmark for evaluating simulations of the Arctic radiation budget by previous studies (Boeke and Taylor 2016; Christensen et al. 2016; Huang et al. 2017).

4) EKF400v2 and PHYDA global paleo-reanalysis

We use the EKF400 version 2400-yr paleo-reanalysis reconstruction dataset, which utilizes an ensemble Kalman fitting method to assimilate multiple observations (including instrumental observations, historical climate indices, and proxy data) with the ECHAM5.4 AGCM simulations (EKF400; Franke et al. 2017). This dataset provides monthly 500 hPa geopotential height (Z500) and surface temperatures over the period from 1603 to 2003, which allows us to better examine global circulation variability in each season over the past 400 years. In the ERA-I and EKF400 products, the detrended correlation between JJA Z500 and JJA surface temperature is 0.52 (1979–2018, ERA-I) and 0.59 (1600–1920, EKF400), respectively. The correlation between ERA-I JJA Z500 and NSIDC total September SIA is -0.54 (1979-2018, detrended). Observations and proxy data are taken from only over land. From 1600 to 1800, tree-ring width and maximum latewood density constitute the majority of the assimilated data outside of Greenland and Europe at high latitudes and are only assimilated from April to September. Instrumental station data from southern Greenland and northern Europe become more prominent after 1800 and are available yearround. We compare surface temperatures from EKF400 with those from the Paleo Hydrodynamics Data Assimilation

product (PHYDA; Steiger et al. 2018) to confirm we are obtaining a consistent signal from the proxy data. PHYDA, an updated version of the Last Millennium Reanalysis (LMR2; Tardif et al. 2019), assimilates PAGES2k proxy records into bias-corrected output from the CESM1 Last Millenium Ensemble (CESM1-LME; Otto-Bliesner et al. 2016). The CESM1-LME uses the same model as the CESM1-LE but with ~2° atmosphere and land components. Brennan and Hakim (2022) have used a similar paleoclimate proxy data assimilation framework based on LMR2 in skillful reconstructions of annual mean Arctic sea ice using surface air temperature and sea ice concentration from the same model priors as the two products shown in this study. In these reconstructions much of the variance and skill comes from regions closest to land-based proxy records in the PAGES2k database that are also assimilated into EKF400 and PHYDA, suggesting that the most important information for sea ice reconstructions is coming from these proxies via surface air temperatures, which should lend confidence in establishing the connections between atmospheric circulation and surface changes in the Arctic since the year 1600. This may introduce biases in the reconstruction of sea ice and surface temperature further away from these land-based proxy records, such as in the central Arctic. The sea ice state may have been different prior to the rise of anthropogenic forcing in the mid twentieth century, and the sea ice sensitivity to atmospheric circulation and surface temperature changes may not have behaved exactly as it has in recent decades. When examining these reconstructions, we focus on the 10-yr non-overlapping periods of EKF400 JJA Z500 and its relationship with JJA surface temperatures from EKF400 (r = 0.81) and PHYDA (r = 0.68) as well as annual mean total SIA from Brennan and Hakim (2022, r = -0.52).

c. CESM1.2.2.1 nudging experiment design

1) NUDGING APPROACH

Previous work by Huang et al. (2021), nudging winds in the CESM1 from 2000 to 2016, found an important role of atmospheric circulation variability in contributing to observed lowlevel clouds in the Arctic. Li et al. (2022) and Roach and Blanchard-Wrigglesworth (2022) also used a similar nudging approach to quantify the contribution from wind forcing to recent trends in Arctic upper ocean warming and sea ice, respectively. In this study, we seek to build on the concepts employed in Huang et al. (2021), Li et al. (2022), and Roach and Blanchard-Wrigglesworth (2022) by nudging high latitude winds in the Community Earth System Model version 1.2.2.1 (CESM1, see Table 1; Hurrell et al. 2013) over the period from 1979 to 2018, using the same resolution (\sim 1°) and components as the CESM1-LE (CESM1.1.1), with an emphasis on the sea ice response. The goal of these experiments is to examine the role of tropospheric wind patterns on Arctic sea ice; therefore, we nudge above ~850 hPa, allowing the surface and lower troposphere to interact with one another. This level was decided based on correlations between total September sea ice and Arctic-averaged (70°–90°N) geopotential heights, which are limited to above ~800 hPa in the reanalysis

TABLE 1. Nudging experiment design. Model and nudging specifications for perpetual and continuous nudging simulations in the CESM1.2.2.1 using fixed CO₂ concentrations (367 ppm).

Name	Model	Domain	Reanalysis	Description
Continuous	CESM1.2.2.1	60°-90°N < 850 hPa fixed CO2 (397 ppm)	ERA-Interim, 1979–2018	10-member nudging runs to continuous 40-yr reanalysis record branched from member of CESM1-LE
Perpetual	CESM1.2.2.1	60°-90°N < 850 hPa fixed CO2 (397 ppm)	ERA-Interim, 1979–2018	40-member nudging runs repeating each reanalysis year (1 Jan–31 Dec) for 10–21 model years each from same init. conditions branched from same member of CESM1-LE

(Fig. 3 in the online supplemental material). We find that extending nudging down to the surface does not alter these results or their conclusions (not shown). To nudge the model to ERA-I horizontal winds, we follow the methodology from Blanchard-Wrigglesworth et al. (2021):

$$\frac{dx}{dt} = F(x) + F_{\text{nudge}},$$

$$F_{\text{nudge}} \alpha [O(t'_{\text{next}} - x(t))] / \tau,$$
(1)

where x(t) is the model state vector at the model time step t; F(x) is the internal tendency of the system with no nudging; and F_{nudge} is the nudging term, proportional to the difference between the target analysis (ERA-I horizontal winds) at a future analysis time step, $O(t'_{\text{next}})$, and the model state at the current model time step, x(t). In the atmosphere, the analysis that the model is nudged toward is updated every 6 h (the analysis time step t' next) while F_{nudge} is adjusted at each model time step (in CAM5, $\Delta t = 30 \text{ min}$). The nudging coefficient α is set to an intermediate strength (0.5) everywhere within the nudging domain to further allow the model's own variability to influence the circulation pattern, though the results do not show a sensitivity to nudging factors (ranging from 0 to 1) greater than 0.5 (Huang et al. 2021).

2) CONTINUOUS (10-MEMBER, 40-YR SIMULATIONS)

To examine the model's capability in replicating some features of observed sea ice changes over the past 40 years, we first run a 10-member ensemble of 40-yr continuous simulations with winds nudged to reanalysis from 1979 to 2018 and fixed greenhouse gas concentrations at the level of the year 2000 (367 ppm), which are very close to the mean concentrations of greenhouse gases over the period. These simulations suggest that the model has a reasonable skill to capture some features of the observed sea ice decline since 1979 under continuous wind forcing (see section 3a for more details). We test the sensitivity of our wind nudging approach to CO₂ forcing by conducting the same continuous nudging experiments with time-evolving CO₂ concentrations during the period 1979-2018 (not shown). While we find that the overall trends are more negative with increasing CO2 concentrations, the year-to-year variability in total September SIA remains unchanged, suggesting a relatively small influence of CO2 forcing on our analysis of the perpetual wind nudging simulations described in the following section.

3) PERPETUAL SIMULATIONS (40-MEMBER, 10–21-YR SIMULATIONS)

One limitation of the continuous simulation is that it is unclear whether strong melting over some years is due to winds over immediately preceding periods, or an accumulation of changes induced by winds occurring previously. Arctic sea ice likely has memory that can last for several years through the persistence of thickness changes and absorption of heat in the ocean that can complicate our understanding of the sea ice response to wind patterns associated with a specific year (Blanchard-Wrigglesworth et al. 2011; Tietsche et al. 2011). Repetitively forcing the model with winds from the same year may overcome this limitation and provides a new opportunity to search the optimal internal mode favoring the strongest sea ice melting.

To do so, we separate the ERA-Interim record into individual years and conduct 40 additional perpetual simulations using the same configuration (Table 1; e.g., the nudging parameter and domain, and anthropogenic forcing: year 2000). In each simulation, the model is integrated for 10 years, with atmospheric circulation within the Arctic (60°-90°N) repeatedly nudged to the ERA-Interim 6-hourly wind field from an individual year in the reanalysis. All simulations are initialized from identical conditions, branched from the same member of the CESM1-LE that is representative of moderate conditions in terms of its sea ice area and volume in 2000/1/1 among a total of 40 members. By repeating the same wind pattern for consecutive model years, the responses of sea ice and other characteristics of the Arctic climate to circulation changes are enhanced, making them easier to differentiate from confounding processes. We can then better assess the mechanisms resulting from atmospheric circulation variability affecting Arctic sea ice cover at the end of the melt season for each year. This perpetual approach also partially compensates for issues associated with initialization, since memory associated with initial conditions is likely limited to 3-4 years (Blanchard-Wrigglesworth et al. 2011), and greenhouse gas forcing, which is the same in all runs. Atmospheric carbon dioxide concentrations are fixed at the same concentration as the continuous nudging simulations (367 ppm).

For some perpetual runs that have the strongest melting and strongest growth in September sea ice over the 10 years we extend the simulations to 21 years under wind forcing of the same year [see section 2b(3), Table 2]. For these reanalysis years, extending the length of integration ensures that

TABLE 2. Extreme sea ice years from 10-yr nudging simulations. Composites in Figs. 1–4 are based on the mean of the five low sea ice years minus the mean of the five high sea ice years in total September SIA from the perpetual nudging simulations and NSIDC sea ice concentration product. Low sea ice and high sea ice years are calculated using periods matching ERA-I (1979–2018) and EBAF (2000–18) availability.

Product	Strong melting years ($\leq 1\sigma$)	Strong growth years $(\geq 1\sigma)$
Perpetual nudging	1993, 2007, 2011, 2012, 2015	1996, 2001, 2002, 2010, 2017
NSIDC (detrended, ERA-I years)	1979, 1990, 2007, 2008, 2012	1992, 1994, 1996, 2001
NSIDC (detrended, EBAF years)	2007, 2008, 2012	2001, 2014

Arctic sea ice has stabilized in response to the nudged wind patterns and provides a quasi-equilibrium response to imposed wind forcing.

4) COMPOSITES OF PERPETUAL NUDGING SIMULATIONS AND REANALYSIS

Composites are made based on the 10-yr means of the low sea ice years [less than -1 standard deviation (std) of ensemble September SIA] minus the high sea ice years (greater than +1 std ensemble September SIA) from the perpetual nudging simulations. The results are not sensitive to using the 10-yr linear trends or the last year total September SIA from each simulation. The preceding months (January-May) and summertime (JJA) geopotential height, temperature, long-/ shortwave radiative fluxes, top/bottom/lateral melting, and thermodynamic/dynamic tendencies are composited based on the low sea ice minus high sea ice years. For the preceding months we use January-May because the repetition of reanalysis years may introduce a discontinuity in the nudged winds at the beginning of each calendar year. However, we use a nudging strength of 0.5, giving the model some flexibility to handle this transition and there is no clear indication of this discontinuity in the simulated sea ice (supplemental Fig. 1). Because rapid sea ice decline is one of the most pressing concerns of recent climate change, we focus the framing of our analysis of composites on the processes contributing to enhanced melting, but one can consider the reverse to be conducive for sea ice expansion. Statistical significance of the composites is determined using a two-sample Student's t test. For ERA-Interim composites we use the same approach based on the low sea ice years minus high sea ice years (±1 std) in detrended total September SIA from the NSIDC sea ice concentration product. The low sea ice years derived from detrended NSIDC September SIA are 1979, 1990, 2007, 2008, and 2012. The high sea ice years are 1992, 1994, 1996, and 2001 (Table 2). Since EBAF is only available from 2000 to 2018, we recalculate these low sea ice years and high sea ice years based on the 19 years detrended NSDIC data using the same criteria (± 1 std; Table 2).

3. An optimal sea ice melting mode in the nudging simulations

a. Strong and weak sea ice melting years determined by different wind patterns

We first examine the continuous 40-yr simulation [see methods, section 2b(1)] using the same nudging domain and

fixed greenhouse gas concentrations (Fig. 1a) but with nudged winds varying from 1979 to 2018. The continuous simulations agree well with observed sea ice changes from the NSIDC (detrended r = 0.58, raw r = 0.65, Fig. 1a). Considering the optimal conditions for low Arctic sea ice years, the imposed wind patterns in the continuous 40-yr simulations capture many of the important features of total September SIA observed in recent decades (extreme years, rapid decline from 1996 to 2012, year-to-year fluctuations, significant decline since the early 2000s). The nudging simulations deviate from the observed sea ice changes in the early 1990s, possibly due to a lack of aerosol cooling from the Pinatubo eruption in our wind-only constrained nudging simulations (Lehner et al. 2015; Yang et al. 2019; Brennan and Hakim 2022), the use of year 2000 initial conditions and CO₂ concentrations, or issues in the assimilated data. During this period there is also an increase in total September SIA in the forced response of the CESM1-LE reflecting a cooling effect from aerosols (green curve in Fig. 1a).

We then separate the wind patterns from each year into its own simulation and repeat the same nudging for 10–21 years to magnify the wind patterns over individual years. This set of experiments will be referred to as the perpetual simulations [see methods, section 2b(2)]. The model exhibits very different behavior across these 40 perpetual simulations with some runs experiencing a strong sea ice decline and some with substantial ice growth. Since the only difference in forcing imposed in these runs is large-scale winds in the Arctic, the bifurcation of these sea ice changes is primarily due to wind forcing.

In the perpetual nudging simulations, sea ice responds quickly to changes in atmospheric forcing. As can be seen by first year total September SIA between the different runs (Fig. 1a), sea ice characteristics diverge within the initial year in response to wind forcing. This difference increases to around 4 million km² in the first 10 years when repeating these wind patterns (red lines in Fig. 1b). The largest observed declining trend over any periods long than 10 years in total September SIA (-2.0 million km² decade⁻¹) is from 2000 to 2012 (black line in Fig. 1a), which is well captured by the perpetual nudging experiments (blue line in Fig. 1a), with the largest 13-yr declining trend (2000-12, blue line) in the 10-yr means of the perpetual nudging simulation occurring during the same period with a similar magnitude of -1.7 million km² decade⁻¹. The largest declining trend over any periods longer than 10 years in the ensemble mean of the CESM1-LE is much lower than the observations (-1.1 million km² decade⁻¹) and does not show the rapid acceleration from 1996 to 2012 or the slowed decline

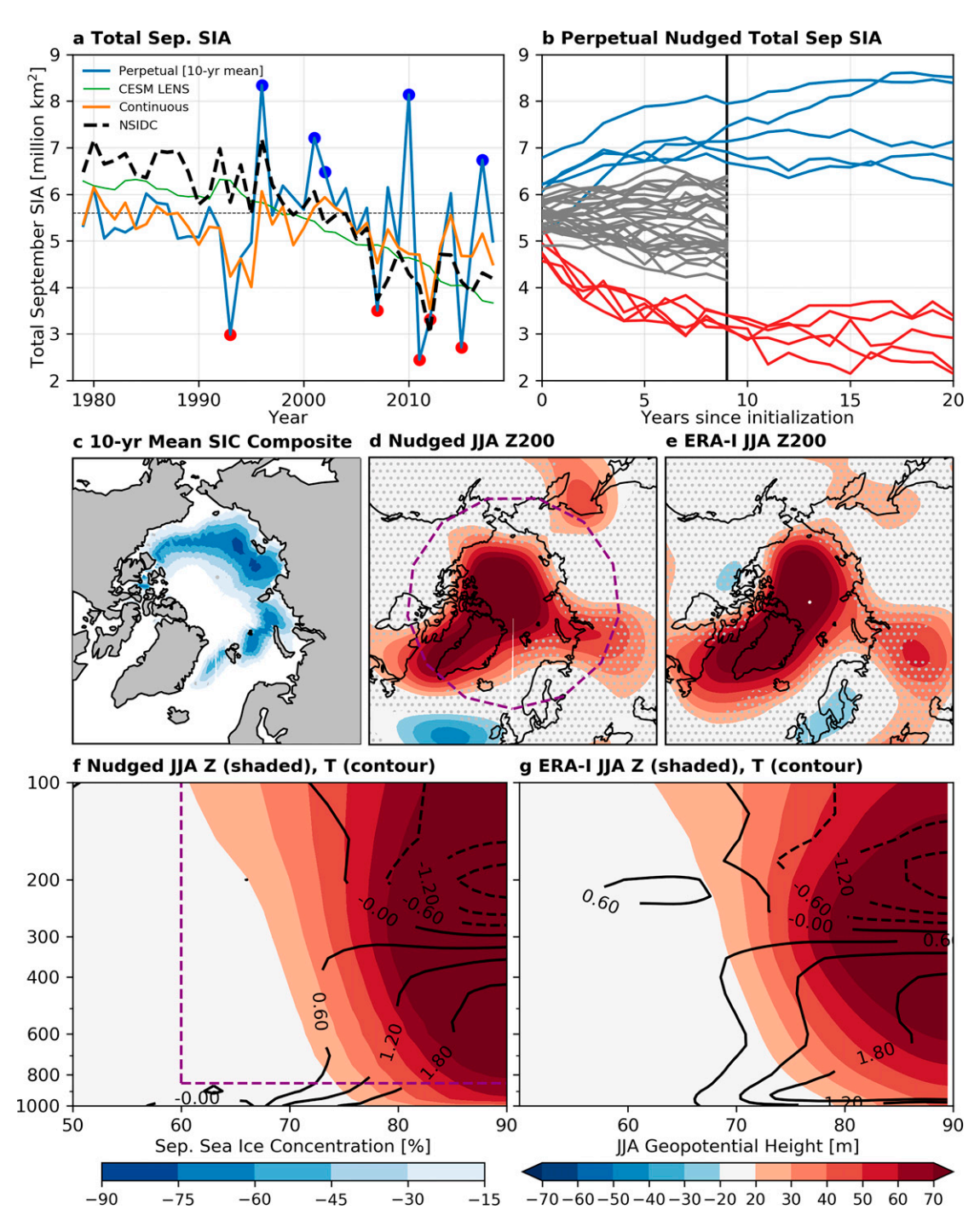


FIG. 1. Composites of nudging simulations and reanalysis. (a) Total September SIA from the CESM1-LE (LENS, green), NSIDC (dashed black), 10-member mean from the continuous simulations (orange), and 10-yr means from the perpetual simulations (blue). In (a), red dots show the low sea ice years and blue dots show the high sea ice years from the perpetual nudging simulations. (b) Total September SIA from the perpetual simulations. In (b), red lines represent the low sea ice group, blue lines represent the high sea ice group, and the gray curves represent all remaining years. (c) 10-yr-mean composites of sea ice concentration, (d) JJA 200 hPa geopotential height, and JJA zonal mean geopotential height (shading) and (f) temperature (contours) based on the years from the low sea ice group minus the high sea ice group in the perpetual simulations [row 1 in Table 2, red minus blue in (a)]. Composites of (e) JJA 200 hPa geopotential height and (g) JJA zonal mean geopotential height (contours) and temperature (shading) based on the low sea ice years minus the high sea ice years in the detrended NSIDC record (row 2 in Table 2). Dashed purple contours indicate the nudging domain within the Arctic $(60^{\circ}-90^{\circ}N)$ and above ~ 850 hPa. Stippling indicates composite differences are not statistically significant at the 95% confidence level based on a two-sample Student's t test.

thereafter as seen in the observations and nudging simulations, indicating that the rise of CO_2 forcing over the same period (around 2 ppm yr⁻¹) cannot solely explain this decline. Instead, the largest 13-yr decline in the CESM1-LE ensemble mean is from 2006 to 2018, likely associated with the sea ice state (Holland et al. 2019) and the transition from historical to RCP8.5 forcing. Year-to-year variability in the 10-yr means from these perpetual nudging simulations also agrees with total September SIA from the NSIDC (detrended r = 0.50, Fig. 1a).

We begin by compositing based on the means of the first 10 years of total September SIA loss in each member of the perpetual simulations. The results are insensitive to the approach for quantifying sea ice loss, with the 10-yr means, 10-yr trends, and final (year 10 or 21) total September SIA, as well as using total sea ice volume or average sea ice thickness. Nudging winds from 1993, 2007, 2011, 2012, and 2015 produce the strongest declines above one standard deviation in total September SIA and are defined as the low sea ice group (Table 2). Though many of the years in the low sea ice group coincide with the lowest observed years, it should be noted that the 2015 and 1993 simulations experienced strong simulated sea ice loss but are not among the lowest recorded years, suggesting there is likely confounding effects from the sea ice and ocean states, previous years, or other unaccounted processes (e.g., moisture and heat transport from the lower latitudes to the Artic by the atmosphere and ocean) in the real world that are critical in determining the observed sea ice state in each year. In addition, low sea ice cases in the perpetual simulations reflect an amplified response of sea ice to specified winds over a 10-yr period in the model. However, in nature, the same wind patterns can only apply this forcing on sea ice in a short 1-yr time window in the presence of many other forcings. This amplification along with fixed greenhouse gas concentrations in the nudging simulations likely explains some of the mismatch in the rankings of these extreme melting years between the simulations and observations.

In the perpetual simulations, nudging winds from 1996, 2001, 2002, 2010, and 2017 generates the strongest growth in total September SIA over 10 years and are defined as the high sea ice group. 1996 stands out as a particularly strong sea ice growth outlier and is the highest recorded total September sea ice year in the satellite record. Four out of the five same years also constitute the low sea ice and high sea ice members in terms of total volume and average thickness of September Arctic sea ice in these simulations (supplemental Fig. 1).

Compositing sea ice concentration based on the sea ice change groups yields a relatively uniform difference across the Arctic, likely resulting from contributions associated with thermodynamic processes (i.e., radiative fluxes, albedo) as well as mechanical break up and export. The composites show the greatest differences in the East Siberian–Laptev–Kara Sea regions and a weak increasing signal along the eastern coast of Greenland during low sea ice years. These regions with strong sea ice decline in response to wind forcing are also the regions seeing strong sea ice melting trends over recent decades in observations (Baxter et al. 2019).

b. Local atmospheric, radiative, and sea ice melting processes associated with strong melting summers

In observations and the continuous nudging simulations, autocorrelations of total September SIA with SIA in the preceding months only show statistically significant coefficients with June-August (JJA) sea ice (supplemental Fig. 2). In the nudging simulations, there is a statistically significant pattern in regressions of observed JJA Arctic geopotential height and temperature onto total September SIA but no statistically significant pattern in January-May (supplemental Fig. 3). This phenomenon has been referred to as the spring predictability barrier for September Arctic sea ice (Bushuk et al. 2020). To maintain consistency with the observed relationship, we focus on JJA atmospheric circulation. Composites of JJA 200 hPa geopotential height in both the perpetual nudging experiments and ERA-I, constructed using the definition of the low sea ice and high sea ice years (Table 2), show a prominent "Figure-8" anticyclonic patterns with centers over southwest Greenland and the central Arctic in the strongest melting years relative to the sea ice growth years consistent with the regression pattern from ERA-I (Figs. 1d,e). Friction at the surface of the anticyclone generates large-scale subsidence throughout the mid- to lower troposphere, consistent with the reanalysis, but with differences in the vertical structure near the surface below the nudging domain (Figs. 1f,g). Adiabatic descent of air induces warming and moistening (not shown, Ding et al. 2017) of the lower Arctic atmosphere that then increases the emission of longwave radiation. The strong similarity between the vertical structure of atmospheric fields n the nudging run and ERA-I indicates that wind forcing is critical in governing changes of tropospheric temperature in the Arctic, which is essential for determining radiation in the entire air column, as well as sea ice and upper-ocean temperature variability.

Despite the anticyclonic-dominated regime seen in the composites, there is an increase in low cloud cover along the Eurasian coast (not shown), consistent to the analysis in Huang et al. (2021). Huang et al. (2021) argue that the high pressure may increase the low-level clouds throughout much of the Arctic through advection and subsidence-induced entrainment of moisture into the inversion layers. However, we do not go into detail on cloud radiative effects in these simulations because there are well-documented biases in microphysical and boundary layer processes that may lead to the differences seen between the products (Sotiropoulou et al. 2016; Tan and Storelymo 2019; McIlhattan et al. 2020).

To better understand the radiation balance associated with the melting process in the perpetual nudging runs, we compare the simulated radiation fluxes at the surface and TOA in the Arctic with their observed counterparts in ERA-I and EBAF. Since EBAF is only available after 2000 and the sample size of the extreme sea ice melting/growth years over this period is smaller (Table 2), the composite using EBAF may contain large uncertainty or be biased by changes in certain individual years, and sensor-related artifacts, especially in the computed surface fluxes.

Since the radiation response in our nudging simulations represents an extreme scenario in which winds have a chance to solely regulate the radiation fields over 10 years, there are discrepancies among the three datasets. At the surface, the three products show consistent signals for most fluxes (Fig. 2a; supplemental Fig. 5). Enhanced downwelling LW (LW_{down}) and less reflected SW (SW_{up}) in JJA appear to be the two main components contributing to a gain of heat at the surface, conducive for strong sea ice melting. As expected, JJA atmospheric anticyclonic circulation anomalies can enhance downwelling LW and the ice-albedo feedback is triggered, explaining less reflected SW. The ice-albedo feedback in these simulations also includes conversion of the ice surface from snow to bare ice and melt ponds as the enhanced shortwave absorption is uniformly distributed wherever there is sea ice not just sea ice loss (Figs. 2e,h). In the meantime, the impacts of less reflected SW at the surface are also translated to the TOA to reduce upwelling SW. Thus, the ice-albedo feedback which is triggered by winds plays a key role in determining the radiation balance in the Arctic atmosphere in summer.

To better illustrate the radiation balance at the surface and the TOA, we mainly focus on LW_{down} and SW_{up} at the surface and SW_{up} at the TOA (Figs. 2b-j). Downwelling longwave radiation at the surface is enhanced during years of strong sea ice melting throughout the Arctic in the perpetual nudging simulations and ERA-I (Figs. 2b,c). It is not as strong in EBAF likely due to differing impacts of clouds between these products (Fig. 2d). In the perpetual nudging simulations, strong shortwave absorption occurs throughout the Arctic, wherever there is sea ice or snow cover loss and melt pond formation (Fig. 2e). However, in ERA-I and EBAF, significant surface shortwave absorption primarily takes place in the Beaufort Sea (Figs. 2e,f). EBAF has a stronger signal of shortwave absorption in the Beaufort region than ERA-I near the center of anticyclonic circulation in certain low sea ice years (Kay et al. 2008; Wernli and Papritz 2018). The spatial patterns of SW_{up} at the TOA closely resembles that at the surface (Figs. 2h-j). This signal reaches the TOA throughout the Arctic in the perpetual simulations and in particular the Beaufort Sea in both ERA-I and EBAF. In all products, under the control of strong atmospheric anticyclonic winds during years of summertime sea ice loss, more shortwave absorption at the surface due to the ice-albedo feedback dominates the surface and TOA radiative budgets (Figs. 2e-j).

We separate the shortwave feedbacks resulting from changes in surface albedo and cloud optical properties using the approximate partial radiative perturbation method (APRP, Taylor et al. 2007). The differences between the low sea ice years and high sea ice years are dominated by the surface albedo feedbacks from March to October, peaking in July (Fig. 3). Changes in cloud radiative effects, associated with anticyclonic circulation slightly contribute to increased surface shortwave absorption during June and July, but decreased absorption in August, that may be associated with decreased cloud cover above 900 hPa (Huang et al. 2021). Over 20 years of the perpetual simulations, the surface albedo feedback more than doubles, while the cloud and atmospheric components remain relatively small (Fig. 3b).

Next, we shift our focus to the melting processes that contribute to decreased surface albedo through strong sea ice loss in the perpetual nudging simulations as these processes cannot be easily quantified from available observations and reanalysis. In low sea ice years, top melting primarily occurs near the sea ice edge in June and throughout the Artic during July in response to warmer temperatures, downwelling longwave radiation, and shortwave absorption (Fig. 4). Years with the most extreme top melting in July coincide with the same years that are in the low sea ice and high sea ice years in terms of total September SIA, leading to a difference in melting of up to 1.5 cm day⁻¹ in the Pacific Arctic. This correspondence with total September SIA is not seen in other months or in bottom and lateral melting, indicating that July is the month in which the ice-albedo feedback is the most active and sensitive, as it coincides with the peak of incoming solar radiation at the TOA and the mean state of sea ice is thinner and more fragile (little snow, extensive melt ponds).

Bottom melting, in contrast to top melting, occurs at a weaker magnitude (up to 1 cm day⁻¹) and in the later stages of the melt season as the ocean takes more time to absorb shortwave radiation and warm (Figs. 4d-f) due to its large heat capacity. Shortwave absorption and melting are also enhanced by ice mass transport in the Pacific sector that breaks up the ice pack and exposes open ocean in the Beaufort Sea (purple vectors in Fig. 4). Sea ice export into the Atlantic increases slightly as the sea ice is thinned and primed for movement in response to perpetual wind forcing following a similar pattern as the 10-yr means (Figs. 5d-f).

Composite analysis of the perpetual nudging simulations highlights a leading role of wind-driven radiative impacts relative to dynamics on Arctic sea ice loss; however, in most studies, the loss of sea ice due to winds is generally examined in the context of these dynamical effects, specifically export of sea ice out of the basin. But by using the partitioning of sea ice volume tendency into thermodynamic and dynamic components we find in low sea ice years there is weak sea ice export through the Fram Strait during July, and little to none in other months (Fig. 5). The strong anticyclonic ice mass transport during July also leads to a convergence of sea ice within the central Arctic and along the eastern coast of Greenland (Fig. 5e; Thorndike and Colony 1982). The pattern of the thermodynamic tendency term coincides with that of top melting in June and July, contributing to as much as 2.5 cm day⁻¹ of melting, as well as to bottom melting in August (Figs. 5a-c). During JJA, thermodynamics contribute to 91% of the total volume change relative to dynamics (Fig. 5) with dynamically driven convergence of the ice resulting from anticyclonic circulation producing increasing sea ice volume in the central Arctic. Therefore, the thermodynamic component associated with horizontal temperature advection and shortwave absorption triggered by adiabatic processes should be accounted for as it plays a leading role in wind-driven forcing.

4. An optimal sea ice melting mode in a preindustrial run and paleoclimate reanalysis

Results from the nudging simulations suggest that the CESM1 can capture many of the observed changes in September sea ice

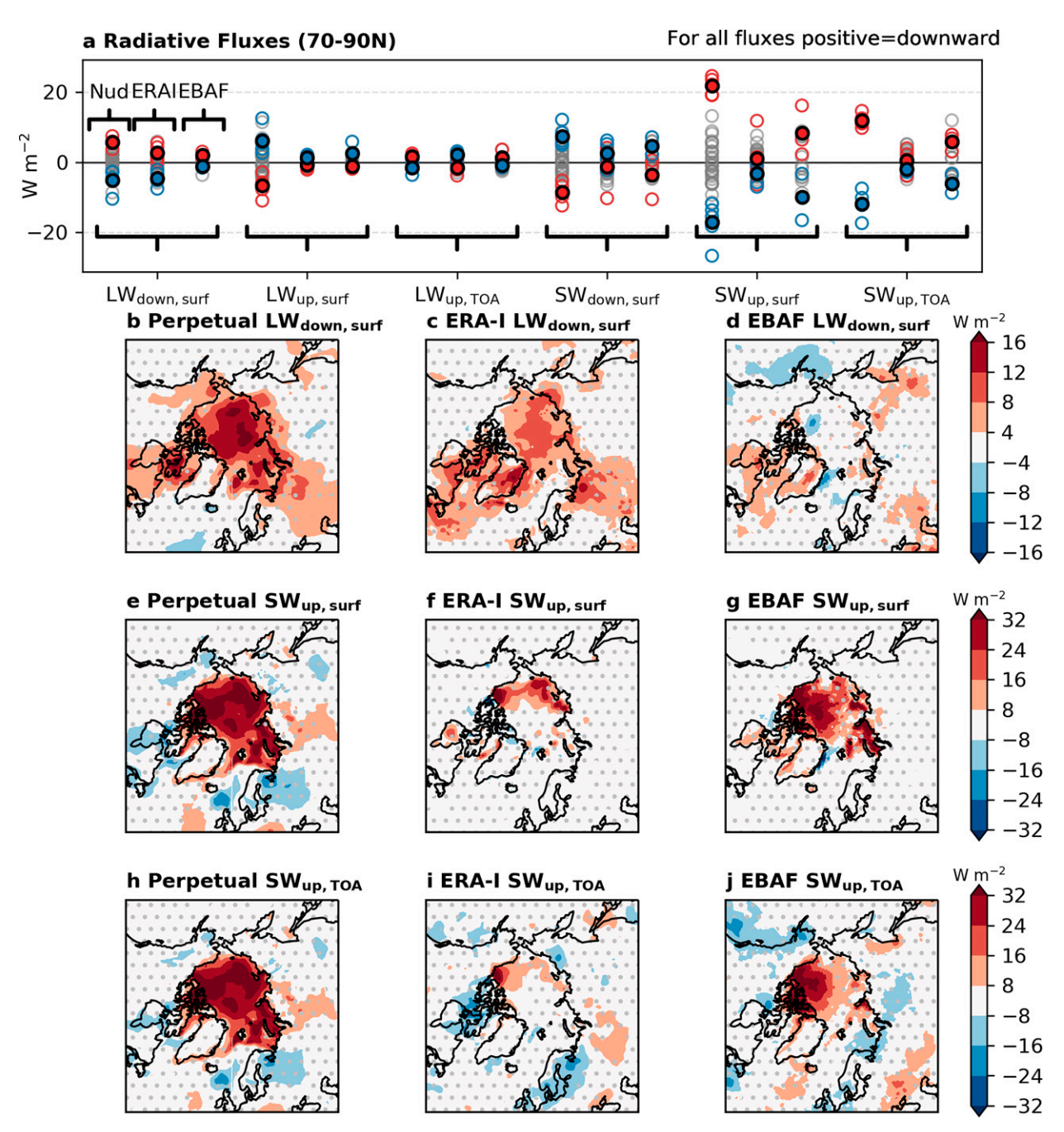


FIG. 2. Surface radiative flux response to nudged winds. (a) JJA surface and TOA radiative fluxes averaged within the Arctic $(70^{\circ}-90^{\circ}N)$ from the perpetual nudging simulations, ERA-Interim, and EBAF. Filled circles indicate low sea ice (red) and high sea ice (blue) group means. Low sea ice years minus high sea ice years JJA (b)–(d) downwelling surface longwave, (e)–(g) upwelling surface shortwave, and (h)–(j) upwelling TOA shortwave radiative fluxes from (left) the perpetual nudging simulations, (center) ERA-Interim, and (right) EBAF. Stippling in (b)–(j) indicates where differences are not statistically significant at the 95% confidence interval according to a two-sample Student's t test. Groups for low sea ice years and high sea ice years are based on years listed in Table 2. For all fluxes shown here, positive values indicate downward fluxes into the surface.

over the last 40 years once winds are constrained to reanalysis data. Since the 40-yr reanalysis is likely too short to cover all possible internal wind variability and the increased anthropogenic forcing over this period may be imprinted in these wind

patterns, we need to search for a similar optimal mode in a longer simulation and reanalysis product containing a broader spectrum of internal climate variability and less influence of anthropogenic forcing. To achieve this goal, we first examine the

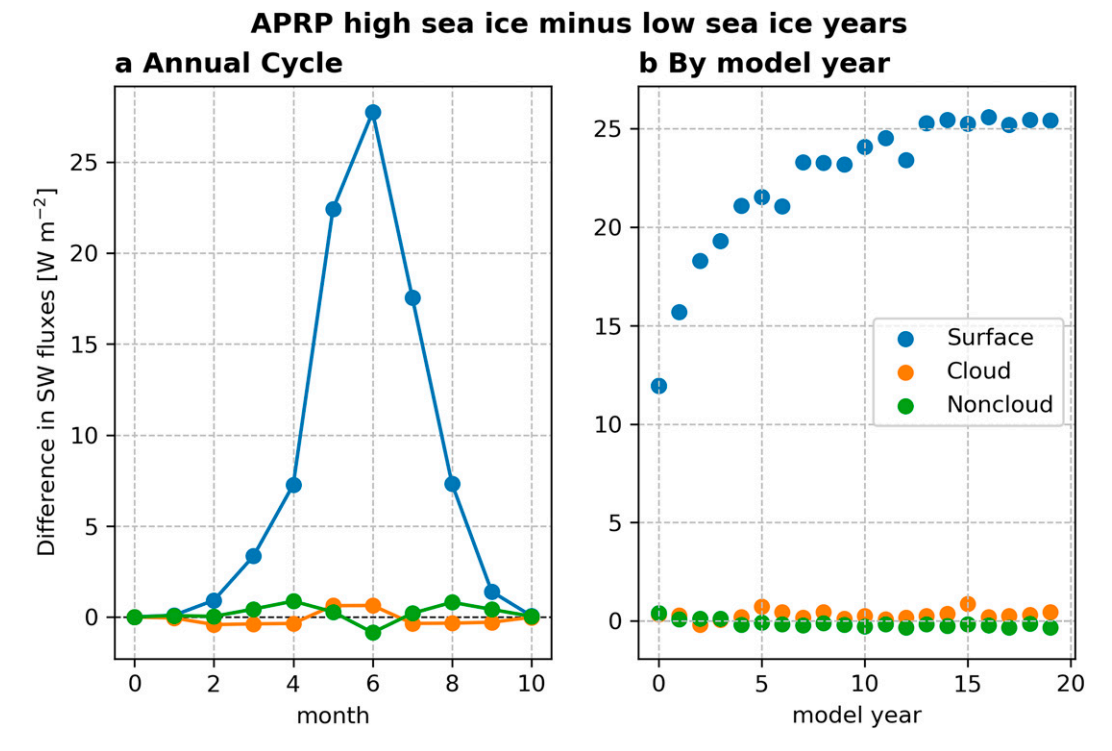


FIG. 3. APRP differences in low sea ice minus high sea ice years. (a) Monthly differences in surface, cloud, and atmospheric scattering/absorption obtained using APRP analysis between low sea ice and high sea ice years from the last 10 years of the perpetual simulations. (b) APRP differences in surface, cloud, and atmospheric scattering/absorption between low sea ice and high sea ice years for each year of the perpetual nudging simulations.

relationship between local Arctic atmospheric circulation and sea ice in a long preindustrial control simulation without anthropogenic forcing.

We take a pseudo-ensemble approach, dividing the 1800-yr CESM1 preindustrial control simulation into non-overlapping, running 10-yr means and composite based on the five low sea ice periods minus the five high sea ice periods for comparison with the 10-yr nudging experiments (Fig. 6a). We also test the sensitivity of our criteria by selecting more members in the extreme groups (e.g., 8, 10, etc.) and find that the composite results show consistent features regardless of group size. We continue focusing on summertime (JJA) since that is the primary season linked with September sea ice.

The CESM1 preindustrial control simulation is able to capture a similar structure over the Arctic basin to the nudged simulations, showing high pressure over the central Arctic during years of the strongest sea ice decline (Fig. 6). This comparison serves as an independent test of the model dynamics, suggesting that the processes linking winds and sea ice seen in the nudging experiments are not an artifact of the nudging method but inherent to the model itself and constrained by reanalysis winds. The preindustrial control simulation shows a high pressure system confined to the Beaufort high region during 10-yr periods of low sea ice cover but has a much weaker magnitude of geopotential height rise compared with the composites from the nudging simulations. Similar

magnitudes of sea ice change coinciding with weaker circulation changes may be due to the free running model's ability to sustain very high JJA geopotential height rise over a 10-yr period or coupling between the atmosphere and surface. In the nudging simulations, we force the model to experience this strong 10-yr wind pattern continuously. A period of 10 or more years with sustained wind forcing in the free run would likely need to be sourced either from the local or lower latitude oceans but models have been shown to not accurately capture tropical forcing and may not be able to capture this strong height rise despite a similar circulation-sea ice relationship strength (Topál et al. 2020). However, the local geopotential height changes relative to total SIA change yields similar magnitudes in the 10-yr mean of the perpetual nudging simulations (72 m height rise versus 3.1 million km² melt) and preindustrial control simulation (25 m height rise versus 1.1 million km² melt). The zonal mean temperatures are also similar to those from the nudging simulations, suggesting that the differences in lower tropospheric temperatures between the nudging simulations and ERA-I are not associated with the nudging but due to a surface-driven or boundary layer response inherent to the CESM1. Therefore, the model is still determining this sea ice response to wind forcing and the nudging is only providing a realistic forcing.

We also use the same non-overlapping, running 10-yr window to find a single 10-yr period with the largest decline out

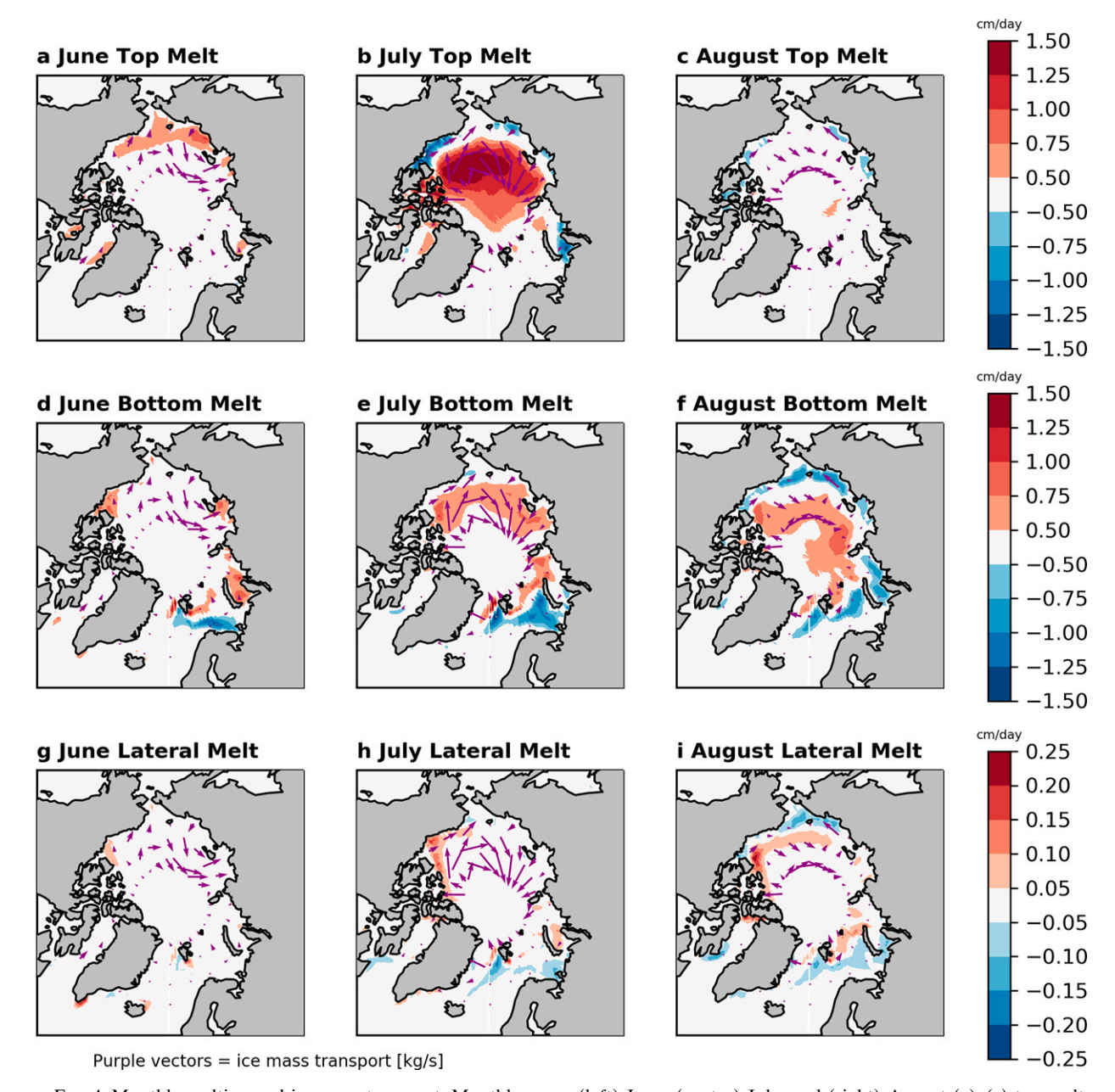


FIG. 4. Monthly melting and ice mass transport. Monthly mean (left) June, (center) July, and (right) August (a)–(c) top melt (units: cm day $^{-1}$), (d)–(f) bottom melt (units: cm day $^{-1}$), and (g)–(i) lateral melt (units: cm day $^{-1}$) in the low sea ice minus high sea ice total September SIA years from the perpetual nudging simulations. Purple vectors show 10-yr-mean ice mass transport (units: kg s $^{-1}$) based on the same composites as melting.

of the entire integration (Figs. 6d,e). The most extreme event shows a very similar structure to the composites and observations, but the magnitude is still half that in observations and the center of high pressure is shifted toward the central Eurasian coast. The "Figure-8" anticyclonic circulation pattern is the optimal mode in the free run, similar to the pattern in ERA-I, suggesting that the observed optimal mode is robust and can exist without CO₂ forcing. Furthermore, the CESM1 can capture the relationship between the strongest

sea ice melting and high pressure over the Arctic. The shifted high pressure system toward the Eurasian coast and over the ice-free ocean surface, produces a zonal mean temperature profile much more consistent with ERA-I, where there is not a surface-driven warming response at the periphery of the basin.

In addition to the CESM1 preindustrial control simulation, we use the same compositing approach and linear detrending to examine two climate proxy-assimilated reanalysis simulations,

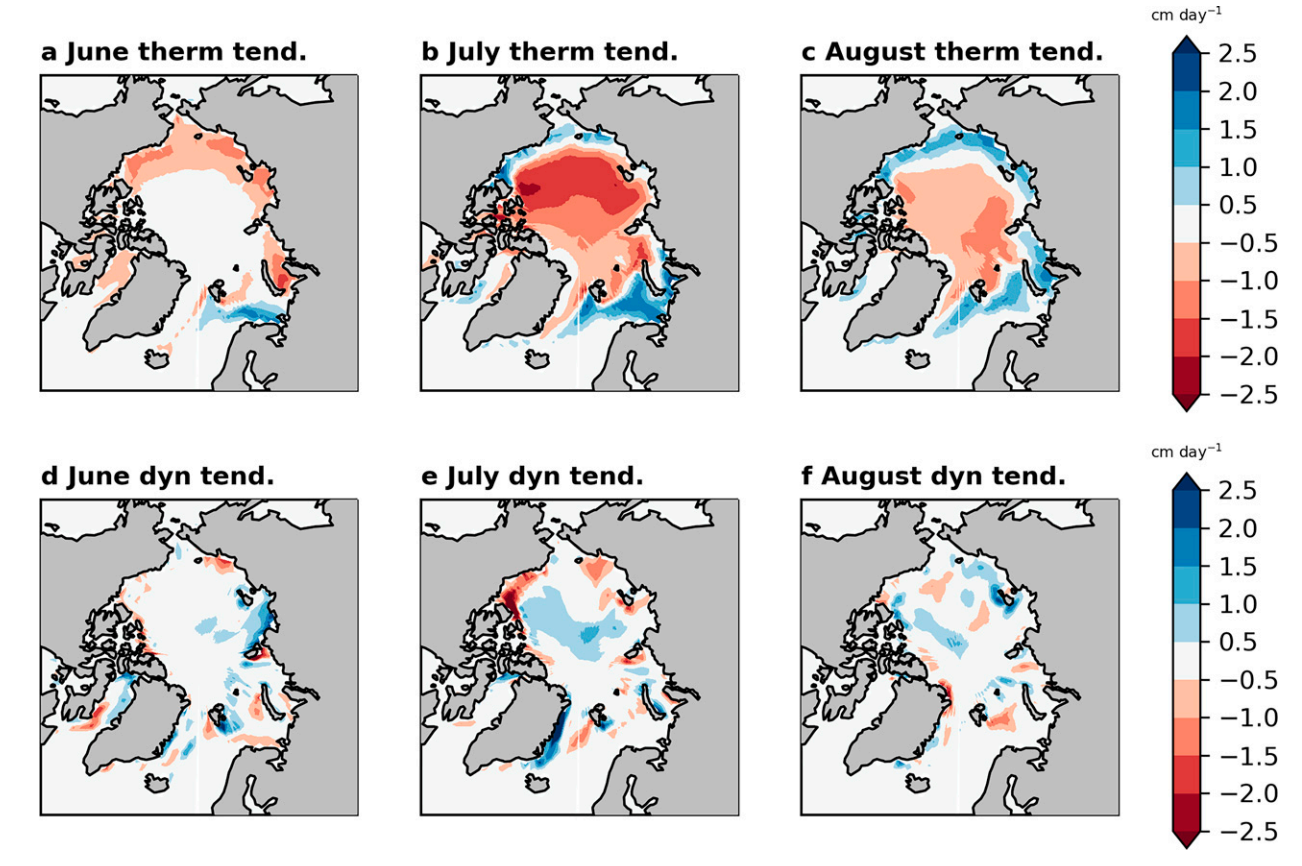


Fig. 5. Monthly volume changes due to thermodynamics vs dynamics. Monthly mean (left) June, (center) July, and (right) August (a)–(c) thermodynamic sea ice volume tendency (units: cm day⁻¹) and (d)–(f) dynamic sea ice volume tendency (units: cm day⁻¹) in the low sea ice minus high sea ice total September SIA years from the perpetual nudging simulations. Note that the colors are flipped relative to the values in Fig. 4 to maintain correspondence between melting and volume/thickness tendency.

EKF400 and PHYDA, as well as a sea ice reconstruction from Brennan and Hakim (2022), to further establish the relationship between atmospheric circulation and sea ice changes over the last 400 years (Fig. 6). We compare EKF400 JJA 500 hPa geopotential heights with the optimal circulation pattern from the perpetual nudging simulations, though it should be noted that EKF400 uses an AMIP-style approach with prescribed sea ice that may lead to errors in surface temperature through the omission of important surface-based feedbacks (Graff et al. 2019). Composites are made using surface temperature because paleo-reanalysis products generally do not include sea ice output due to the rarity of sea ice proxy records. By using surface temperature from the three products, we aim to give more weight to the assimilated PAGES2k paleo-records and reduce some of the uncertainty from model related biases. In addition, JJA Arctic surface temperature (70°-90°N) in the modern era reanalysis and the nudging experiments strongly correlates with total September SIA (r = -0.895 in nudging simulations, Olonscheck et al. 2019, Bonan et al. 2021a). Wang et al. (2021) also used a sea ice model simulation driven by near-surface air temperatures to indicate that September sea ice closely follows changes in 2 m temperature in summer. Thus, we believe that JJA surface temperature variability within the Arctic may

reflect changes of sea ice in summer to a certain extent. Composites of surface temperature based on surface temperature from both EKF400 and PHYDA show consistent centers of warming near the Canadian archipelagos and central Eurasia, though the magnitudes in EKF400 are much smaller (supplemental Fig. 8). EKF400 Z500 composites, despite not including proxy data in or closely around the Arctic, are able to capture a similar JJA high pressure center in Z500 over the Canadian archipelagos and western Greenland that extends into the central Arctic and over the Ural Mountain region in years that have higher surface temperatures (Fig. 7). If the observed relationship between sea ice, surface temperature, and atmospheric circulation observed during recent decades holds, these paleo-reanalyses suggest that a similar mode may have contributed to extreme sea ice loss in the last 400 years in the absence of rapidly increasing carbon dioxide concentrations.

5. Discussion

a. Sensitivity of sea ice to internal circulation forcing

Currently the common practice for quantifying internal variability associated with a model is carried out using a long preindustrial control simulation or large ensembles (Deser et al. 2020).

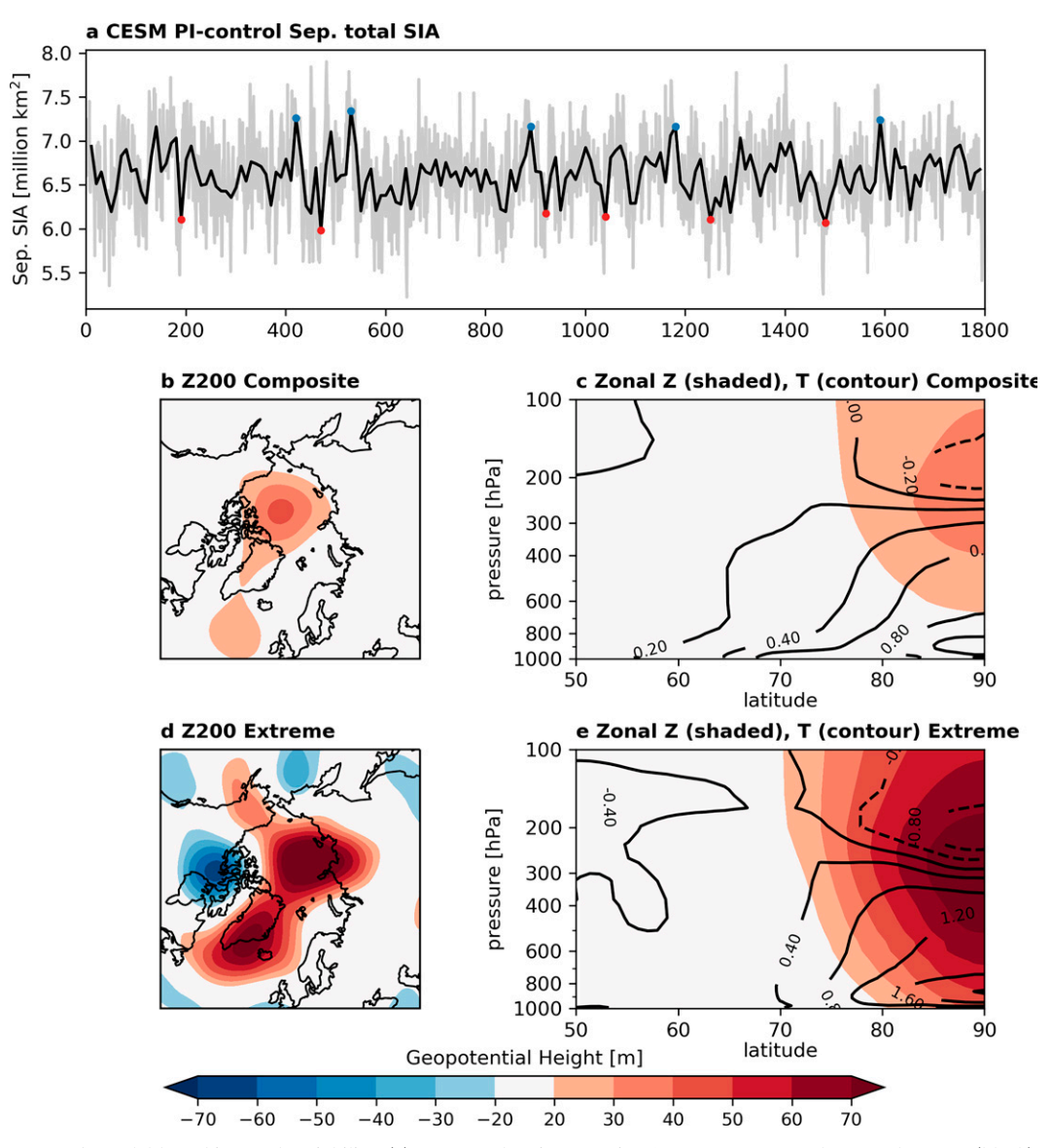


FIG. 6. Model-based internal variability. (a) Non-overlapping, running 10-yr means of total September SIA (black) and its raw year-to-year variability (gray). Red dots indicate lowest total September SIA years over non-overlapping 10-yr periods and blue dots indicate the highest total September SIA 10-yr periods. (b) JJA 200 hPa geopotential height and (c) zonal mean geopotential height (shading) and temperature (contour) from low minus high total September SIA 10-yr periods from the 1800-yr CESM1 preindustrial control simulation. Extreme or optimal (d) Z200 and (e) zonal mean geopotential height pattern favoring the strongest 10-yr September sea ice melting period in the CESM1 preindustrial control simulation. The extreme melting pattern is multiplied by 2 for comparison with the composites of the low sea ice minus high sea ice years from the perpetual simulations.

In this approach, internal variability is determined by model physics and coupling among different components of the system. However, models still have deficiencies in their ability to simulate important relationships between sea ice and the atmosphere, as well as teleconnections between high latitude circulation and remote forcing (Ding et al. 2014, 2017; Rosenblum and Eisenman 2016; Luo et al. 2021). By nudging winds, we can overcome these hurdles to some degree and more effectively evaluate the climate response to

atmospheric variability in a manner more representative of observed rather than model-dependent variability. The composites using the preindustrial control simulation, which are representative of the inherent wind forcing pattern most conducive to enhanced sea ice loss, show an ability to capture many of the observed relationships between the Arctic atmosphere and sea ice.

Due to difficulties with model limitations, previous studies have often focused on a qualitative relationship between

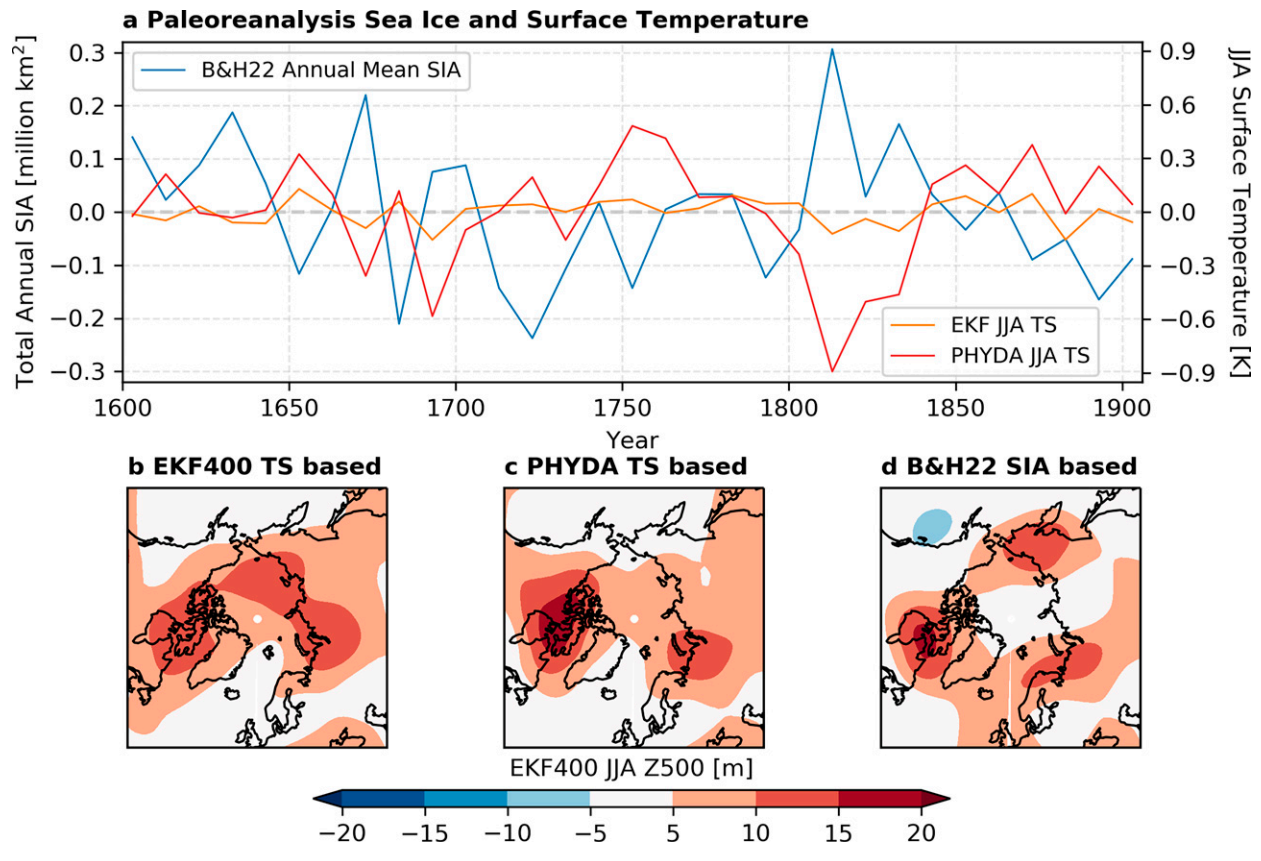


FIG. 7. Influence of wind forcing on Arctic sea ice in paleoreanalysis. (a) Detrended annual mean total SIA reconstruction from Brennan and Hakim (2022) and Arctic-averaged (70° – 90° N) surface temperatures from EKF400 and PHYDA paleoclimate reanalysis. Composites of Z500 (shading) based on the most extreme non-overlapping 10-yr periods from Arctic-averaged (b) EKF400 JJA surface temperature, (c) PHYDA JJA surface temperature, and (d) Brennan and Hakim (2022) annual mean total SIA. In the nudging experiments, JJA Arctic surface temperature (70° – 90° N) strongly correlates with total September SIA (r = -0.895), indicating that pan-Arctic JJA surface temperature can be used as an approximation of September sea ice variability.

circulation and sea ice. This information is important but insufficient for us to understand the detailed sensitivity of September sea ice to preceding JJA circulation change. To achieve a better quantification of this sensitivity we calculate the slope of the linear regression between total September SIA and the preceding JJA Z200 within the Arctic (70°–90°N) and use this slope as a measure of the sensitivity (Fig. 8). This slope (km² m⁻¹) will tell us the extent a higher Z200 rise in m (indicating a warmer atmosphere below 200 hPa) could induce a certain areal change in summertime sea ice. In both the continuous nudging and preindustrial control simulations, the mean sensitivities (7700 and 6600 km² m⁻¹, respectively) are slightly lower than in observations (9000 km² m⁻¹), though the observed sensitivity falls within the spread of all three simulations. The continuous nudging simulations, with a nudging strength of 0.5, reduce the spread in sea ice sensitivity to wind forcing in half relative to the preindustrial control simulation. When conditions favoring strong melting or growth are allowed to persist, such as in the perpetual simulations, the response of sea ice to wind forcing saturates at a little over 20 200 km² m⁻¹, which is over double that of observations and 3 times the continuous and preindustrial

control simulations. The much higher sensitivity later in the perpetual simulations suggests that if the optimal circulation pattern could last longer in the CESM1, as done in the perpetual nudging simulations, the sea ice becomes more responsive to wind forcing through the ice–albedo feedback. However, this effectiveness of this mechanism will be saturated with the upper bound at 23 500 km² m⁻¹ after 5–6 years even if the optimal wind pattern could persist continuously.

The nudging approach, where wind patterns from each year are repeated, also provides novel insight into the role of wind forcing on the ice-albedo feedback. Surface shortwave absorption leading to polar amplification is generally attributed to the consistent and increasing influence of anthropogenic forcing (Curry et al. 1995). However, it should be considered that these model simulations show observed wind patterns are similarly capable of modulating the radiative fluxes entering and leaving the Arctic surface and producing an ice-albedo feedback over several years of persistent, favorable atmospheric conditions for melting. This is important because there are sources of interannual-to-decadal variability, such tropical-Arctic teleconnections, that can generate successive years of wind patterns favoring strong melting (Screen and Deser 2018;

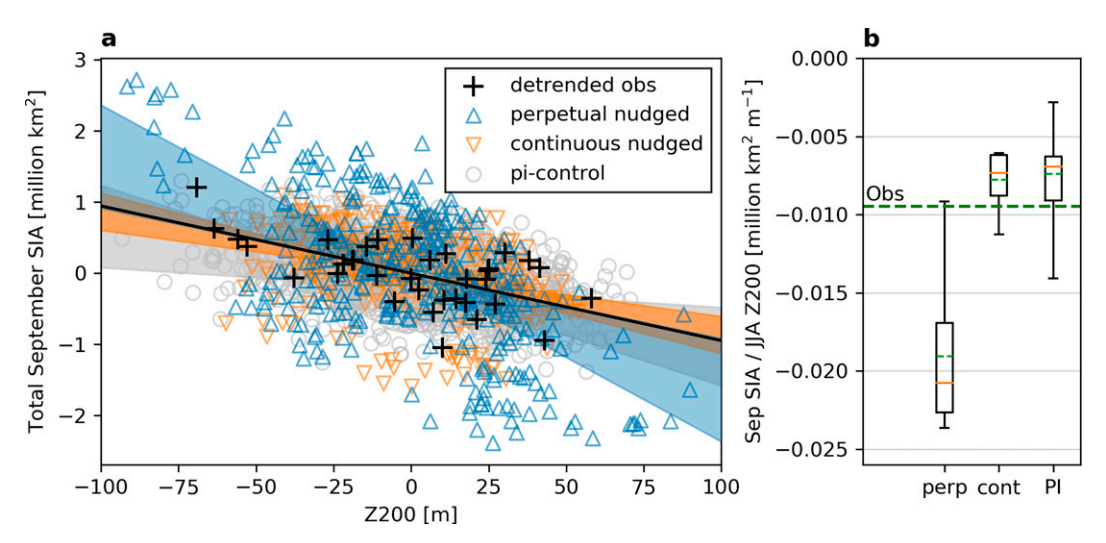


FIG. 8. Observed and simulated sea ice sensitivity to wind forcing. (a) Relationship between JJA Z200 within the Arctic (70°–90°N) and total September Arctic SIA from the detrended ERA-Interim and NSIDC products (black), all years from the perpetual nudging simulations (blue), continuous nudging simulations (orange), and CESM1 pi-control simulation (gray). Shaded envelopes show the range of SIA regressed onto Z200 from each member or pseudomember in the simulations. (b) Regression slopes of total September SIA onto Z200 in the observations (dashed green line), perpetual simulations, continuous simulations, and pi-control simulation. Dashed green lines in boxes show ensemble mean and orange lines show ensemble medians.

Meehl et al. 2018; Baxter et al. 2019; Bonan and Blanchard-Wrigglesworth 2020; Topál et al. 2020). Separating this contribution of internal variability from that of anthropogenic forcing is important for quantifying future trends in melting and warming within the Arctic.

b. Possible caveats associated with the nudging approach

Previously, Huang et al. (2021) found improved agreement relative to satellite-constrained products of cloud changes using the wind nudging approach, as weak air-sea gradients during the melt season generate very little surface influence on cloud changes leaving large-scale circulation as a dominant driver (Kay et al. 2016; Morrison et al. 2019). However, constraining large-scale atmospheric dynamics cannot alleviate all the biases associated with the representation of cloud physics or boundary layer schemes needed to fully understand their role in modulating radiative fluxes and therefore sea ice changes (Huang et al. 2021; Luo et al. 2021). The CESM1, like most Earth system models, has been shown to underestimate supercooled cloud liquid in the Arctic, likely resulting in the small influence of cloud shortwave feedbacks relative to surface albedo in our perpetual simulations (Cesana et al. 2012; Middlemas et al. 2020; McIlhattan et al. 2020).

It is also possible that the arbitrary initialization on 1 January used here introduces inconsistencies, especially when repeated over 21 years, that could impact aspects of preconditioning and seasonal transitions that were not assessed in this study (Stroeve et al. 2014; Smith and Jahn 2019). Composites of the preceding January–May averaged geopotential height and temperature based on the same extreme nudging years from the perpetual simulations (row 1 in Table 2) reproduces a very prominent positive NAO pattern and warming over Siberia, referred to as

the warm Arctic-cold Eurasia (WACE) pattern (supplemental Fig. 6, Mori et al. 2014; Labe et al. 2020). A similar pattern can also be seen in composites using the CESM1 preindustrial control simulation (supplemental Fig. 7), but not in the reanalysis using the extreme detrended years from the NSIDC record (row 2 in Table 2). Features of this predominantly wintertime pattern have been linked to the atmospheric response to sea ice loss, but the physical mechanisms explaining the relationship found here are not well understood (Ogi et al. 2003; Nakamura et al. 2015; Banerjee et al. 2021). It remains uncertain whether this discrepancy is introduced by our arbitrary initialization on 1 January and how important this WACE pattern is in driving summer sea ice. These questions are beyond the scope of this study's experimental framework, but this result should garner further attention and modeling studies in the future.

Another caveat of the approach is that the reanalysis fields are regridded to the nominal 1° resolution of the model. Therefore, nudging to higher resolution reanalysis, such as ERA5, may capture finer resolution processes (Smirnova and Golubkin 2017), though improvement may be limited within our current model setup. Finer model resolution may improve the representation of cyclones in the nudging simulations, which may have had an impact during years with strong cyclonic activity late in the melt season, such as 2012 (Simmonds and Rudeva 2012; Yamagami et al. 2017). Improved simulations of Arctic cyclones or small scale circulations could enhance the dynamical contribution to sea ice loss, in addition to biases associated with the underestimation of sea ice motion (Rampal et al. 2011) or melt pond and thermodynamic parameterization schemes (Keen et al. 2021).

Despite these limitations in the experimental design, the nudging approach used here offers many new opportunities

for further evaluating different climate scenarios in global climate models and responses of a wide array of climate processes (e.g., Arctic Ocean temperature, clouds, high latitude land processes, hydrological and biogeochemical cycles) by partially constraining model dynamics and internal variability to observed or idealized cases over targeted regions. This potential is highlighted by the nudging approach's ability to constrain sea ice in the CESM1 by inducing wind patterns well above the surface and reveals how atmospheric forcing can shape Arctic sea ice variability. Additionally, we focus only on better understanding of interannual variability of summertime Arctic sea ice, but the nudging approach shows tremendous promise in addressing many other processes on a broad range of time scales that contribute to lower atmospheric and surface changes in other seasons and regions as well as improving sea ice forecasts and projections. In particular, this methodology can help us constrain sea ice sensitivity to wind forcing and internal variability within models by quantifying the largest melting response to an optimal atmospheric circulation pattern following complete saturation of the ice-albedo feedback (~25000 km² loss of total September SIA per meter increase in JJA Z200) and can help improve predictions of future changes, such as the first occurrence of an ice-free Arctic.

6. Conclusions

In this study, we conduct a 40-yr continuous simulation and a set of perpetual simulations using the CESMv1.2.2.1, keeping carbon dioxide concentrations fixed and nudging free tropospheric winds within the Arctic (above 850 hPa, 60°–90°N) to those from ERA-I, then repeating each reanalysis year for up to 21 years. Only by partially nudging Arctic winds toward those from ERA-I in the continuous and perpetual nudging simulations, the model can replicate key features of long-term trends and year-to-year changes in total September SIA over the satellite era, despite a slightly weaker relationship between sea ice and winds in the model (Topál et al. 2020). Furthermore, the perpetual nudging simulations allow for the examination of a quasi-equilibrium response of Arctic climate to wind forcing during years of the strongest sea ice change. Four key conclusions were drawn from the perpetual nudging simulations:

- The optimal atmospheric mode that is associated with melt in all datasets is a summertime "Figure-8" quasibarotropic anticyclone centered over the Arctic and extending over Greenland.
- The wind impacts on sea ice are primarily thermodynamic, not dynamic, resulting from subsidence-driven warming of the lower troposphere and the surface icealbedo feedback.
- 3) Sea ice sensitivity to atmospheric circulation change is ~25 000 km² loss of total September SIA per meter increase in JJA Z200, taking ~5-6 years to saturate if the same forcing could be perpetually applied.
- 4) Nudging provides a novel method for studying coupled climate model experiments by constraining atmospheric circulation to examine other components of the Earth system.

In all, this novel application of nudging in a fully coupled climate model shows that the most extreme climate scenario that could cause an abrupt significant sea ice melting epoch is a multiple year-long persistence of the summertime high pressure circulation pattern in the Arctic that enhances a prolonged sea ice-albedo feedback. This pattern can dramatically increase the sea ice sensitivity to internal variability and induce significant Arctic warming. The same process with an opposite sign may also cause a strong recovery of sea ice and a temporary Arctic cooling. In the reanalysis, this optimal mode contributing to sea ice retreat does not occur more than two years in a row. Though infrequent, the CESM1 pi-control simulation and EKF400 experience consecutive years of extreme high pressure over the Arctic greater than +1 std for a maximum of 4 (0.4%) and 3 (3.0%) years in any given 40-yr window, respectively. If considering positive anomalous high pressure over the Arctic (>0 m detrended, 70°-90°N), the maximum consecutive occurrence is 6 (2007-12), 10, and 9 years in ERA-I, the CESM1 pi-control simulation, and EKF400, respectively. Prolonged periods with frequent years characterized by prominent Arctic warming and anomalous high pressure, such as 2007-12, may reflect an emergence of this scenario, which appears to be sensitive to remote forcing over the tropical oceans (Baxter et al. 2019), although this relationship is found to be nonstationary over a longer period (Meehl et al. 2018; Bonan and Blanchard-Wrigglesworth 2020). Thus, the main driving force of this type of persistent anticyclonic circulation pattern in the Artic remains as an important source of uncertainty in projecting future sea ice change. In this study, the nudging approach allows us to control for this uncertainty locally within the Arctic and to directly quantify this relationship using observed atmospheric circulation patterns and may be applied to remote Arctic teleconnections in the future.

Acknowledgments. This study was supported by Climate Variability and Predictability (NA18OAR4310424) and Modeling, Analysis, Predictions, and Projections (NA19OAR4310281) programs as part of NOAA's Climate Program Office, and NSF's Polar Programs (OPP-1744598). We acknowledge the CESM Large Ensemble Community Project and supercomputing resources provided by NSF/CISL/Yellowstone (https://doi.org/10.5065/D6RX99HX). We thank the CESM Polar Climate Working Group for discussion and computing support. We also thank the three anonymous reviewers for their detailed comments and suggestions that have helped to greatly improve this study.

Data availability statement. ERA-Interim data are accessible from the ECMWF website (https://www.ecmwf.int/en/forecasts/datasets/reanalysis-datasets/era-interim). NSIDC sea ice concentration data are accessible using the ftp site (https://nsidc.org/data/seaice_index/archives). CESM-LE historical/RCP8.5 and preindustrial control simulations can be accessed at the UCAR website (https://www.cesm.ucar.edu/experiments/cesm1.1/LE/). EKF400v2 data are accessible from the World Data Center f or Climate (WDCC) at DKRZ archive

(https://cera-www.dkrz.de/WDCC/ui/cerasearch/q?query=*:* &page=0&hierarchy_steps_ss=EKF400) and PHYDA data are accessible from the website (https://zenodo.org/record/1198817#.YPiXEOhKiiM). CESM1.2.2.1 model nudging code and history files are available by contacting the authors. Key output from the nudging simulations used in this study, such as sea ice concentration and geopotential height are available via an OSF repository (https://osf.io/p9t2j/).

REFERENCES

- Banerjee, A., A. H. Butler, L. M. Polvani, A. Robock, I. R. Simpson, and L. Sun, 2021: Robust winter warming over Eurasia under stratospheric sulfate geoengineering—The role of stratospheric dynamics. *Atmos. Chem. Phys.*, 21, 6985–6997, https://doi.org/10.5194/acp-21-6985-2021.
- Baxter, I., and Coauthors, 2019: How tropical Pacific surface cooling contributed to accelerated sea ice melt from 2007 to 2012 as ice is thinned by anthropogenic forcing. *J. Climate*, 32, 8583–8602, https://doi.org/10.1175/JCLI-D-18-0783.1.
- Blanchard-Wrigglesworth, E., K. C. Armour, C. M. Bitz, and E. DeWeaver, 2011: Persistence and inherent predictability of Arctic sea ice in a GCM ensemble and observations. *J. Climate*, 24, 231–250, https://doi.org/10.1175/2010JCLI3775.1.
- —, L. A. Roach, A. Donohoe, and Q. Ding, 2021: Impact of winds and Southern Ocean SSTs on Antarctic sea ice trends and variability. *J. Climate*, 34, 949–965, https://doi.org/10.1175/ JCLI-D-20-0386.1.
- Boeke, R. C., and P. C. Taylor, 2016: Evaluation of the Arctic surface radiation budget in CMIP5 models. J. Geophys. Res. Atmos., 121, 8525–8548, https://doi.org/10.1002/2016JD025099.
- Bonan, D. B., and E. Blanchard-Wrigglesworth, 2020: Nonstationary teleconnection between the Pacific Ocean and Arctic sea ice. *Geophys. Res. Lett.*, 47, e2019GL085666, https://doi.org/10.1029/2019GL085666.
- —, T. Schneider, I. Eisenman, and R. C. J. Wills, 2021a: Constraining the date of a seasonally ice-free Arctic using a simple model. *Geophys. Res. Lett.*, 48, e2021GL094309, https://doi.org/10.1029/2021GL094309.
- —, F. Lehner, and M. M. Holland, 2021b: Partitioning uncertainty in projections of Arctic sea ice. *Environ. Res. Lett.*, 16, 044002, https://doi.org/10.1088/1748-9326/abe0ec.
- Brennan, M. K., and G. J. Hakim, 2022: Reconstructing Arctic Sea ice over the common era using data assimilation. J. Climate, 35, 1231–1247, https://doi.org/10.1175/JCLI-D-21-0099.1.
- Bushuk, M., M. Winton, D. B. Bonan, E. Blanchard-Wrigglesworth, and T. L. Delworth, 2020: A mechanism for the Arctic sea ice spring predictability barrier. *Geophys. Res. Lett.*, 47, e2020GL088335, https://doi.org/10.1029/2020GL088335.
- Cavalieri, D. J., C. L. Parkinson, P. Gloersen, and H. J. Zwally, 1996: Sea ice concentrations from *Nimbus-7* SMMR and DMSP SSM/I-SSMIS passive microwave data, version 1 (NSIDC-0051). NASA/National Snow and Ice Data Center Distributed Active Archive Center, accessed 25 November 2020, https://doi.org/10.5067/8GQ8LZQVL0VL.
- Cesana, G., J. E. Kay, H. Chepfer, J. M. English, and G. De Boer, 2012: Ubiquitous low-level liquid-containing Arctic clouds: New observations and climate model constraints from CALIPSO-GOCCP. *Geophys. Res. Lett.*, 39, L20804, https:// doi.org/10.1029/2012GL053385.
- Christensen, M. W., A. Behrangi, T. S. L'ecuyer, N. B. Wood, M. D. Lebsock, and G. L. Stephens, 2016: Arctic observation

- and reanalysis integrated system: A new data product for validation and climate study. *Bull. Amer. Meteor. Soc.*, **97**, 907–916, https://doi.org/10.1175/BAMS-D-14-00273.1.
- Curry, J. A., J. L. Schramm, and E. E. Ebert, 1995: Sea ice-albedo climate feedback mechanism. J. Climate, 8, 240–247, https://doi. org/10.1175/1520-0442(1995)008<0240:SIACFM>2.0.CO;2.
- Dee, D. P., and Coauthors, 2011: The ERA-Interim reanalysis: Configuration and performance of the data assimilation system. *Quart. J. Roy. Meteor. Soc.*, 137, 553–597, https://doi.org/10.1002/qj.828.
- Deser, C., A. Phillips, V. Bourdette, and H. Teng, 2012: Uncertainty in climate change projections: The role of internal variability. *Climate Dyn.*, 38, 527–546, https://doi.org/10.1007/s00382-010-0977-x.
- —, and Coauthors, 2020: Insights from Earth system model initial-condition large ensembles and future prospects. *Nat. Climate Change*, **10**, 277–286, https://doi.org/10.1038/s41558-020-0731-2.
- Diebold, F. X., and G. D. Rudebusch, 2021: Probability assessments of an ice-free Arctic: Comparing statistical and climate model projections. *J. Econometrics*, https://doi.org/10.1016/j.jeconom.2020.12.007, in press.
- Ding, Q., and Coauthors, 2017: Influence of high-latitude atmospheric circulation changes on summertime Arctic sea ice. Nat. Climate Change, 7, 289–295, https://doi.org/10.1038/nclimate3241.
- —, and Coauthors, 2019: Fingerprints of internal drivers of Arctic sea ice loss in observations and model simulations. *Nat. Geosci.*, 12, 28–33, https://doi.org/10.1038/s41561-018-0256-8.
- —, J. M. Wallace, D. S. Battisti, E. J. Steig, A. J. Gallant, H.-J. Kim, and L. Geng, 2014: Tropical forcing of the recent rapid Arctic warming in northeastern Canada and Greenland. *Nature*, 509, 209–212, https://doi.org/10.1038/nature13260.
- England, M., A. Jahn, and L. Polvani, 2019: Nonuniform contribution of internal variability to recent Arctic sea ice loss. *J. Climate*, 32, 4039–4053, https://doi.org/10.1175/JCLI-D-18-0864.1.
- Fetterer, F., and K. Knowles, 2004: Sea ice index monitors polar ice extent. Eos, Trans. Amer. Geophys. Union, 85, 163–164, https://doi.org/10.1029/2004EO160007.
- Franke, J., S. Brönnimann, J. Bhend, and Y. Brugnara, 2017: A monthly global paleo-reanalysis of the atmosphere from 1600 to 2005 for studying past climatic variations. *Sci. Data*, 4, 170076, https://doi.org/10.1038/sdata.2017.76.
- Graff, L. S., and Coauthors, 2019: Arctic amplification under global warming of 1.5° and 2°C in NorESM1-Happi. Earth Syst. Dyn., 10, 569–598, https://doi.org/10.5194/esd-10-569-2019.
- Graham, R. M., and Coauthors, 2019: Evaluation of six atmospheric reanalyses over Arctic sea ice from winter to early summer. *J. Climate*, 32, 4121–4143, https://doi.org/10.1175/JCLI-D-18-0643.1.
- Holland, M. M., and J. Stroeve, 2011: Changing seasonal sea ice predictor relationships in a changing Arctic climate. *Geophys. Res. Lett.*, 38, L18501, https://doi.org/10.1029/2011GL049303.
- —, L. Landrum, D. Bailey, and S. Vavrus, 2019: Changing seasonal predictability of Arctic summer sea ice area in a warming climate. *J. Climate*, 32, 4963–4979, https://doi.org/10.1175/JCLI-D-19-0034.1.
- Huang, Y., X. Dong, B. Xi, E. K. Dolinar, R. E. Stanfield, and S. Qiu, 2017: Quantifying the uncertainties of reanalyzed Arctic cloud and radiation properties using satellite surface observations. J. Climate, 30, 8007–8029, https://doi.org/10.1175/ JCLI-D-16-0722.1.

- —, Q. Ding, X. Dong, B. Xi and I. Baxter, 2021: Summertime low clouds mediate the impact of the large-scale circulation on Arctic sea ice. *Commun. Earth Environ.*, 2, 38, https://doi. org/10.1038/s43247-021-00114-w.
- Hurrell, J. W., and Coauthors, 2013: The Community Earth System Model: A framework for collaborative research. *Bull. Amer. Meteor. Soc.*, 94, 1339–1360, https://doi.org/10.1175/BAMS-D-12-00121.1.
- Jahn, A., 2018: Reduced probability of ice-free summers for 1.5°C compared to 2°C warming. Nat. Climate Change, 8, 409–413, https://doi.org/10.1038/s41558-018-0127-8.
- —, J. Kay, M. Holland, and D. Hall, 2016: How predictable is the timing of a summer ice-free Arctic? *Geophys. Res. Lett.*, 43, 9113–9120, https://doi.org/10.1002/2016GL070067.
- Kay, J. E., T. L'Ecuyer, A. Gettelman, G. Stephens, and C. O'Dell, 2008: The contribution of cloud and radiation anomalies to the 2007 Arctic sea ice extent minimum. *Geophys. Res. Lett.*, 35, L08503, https://doi.org/10.1029/2008GL033451.
- —, M. M. Holland, and A. Jahn, 2011: Inter-annual to multi-decadal Arctic sea ice extent trends in a warming world. Geophys. Res. Lett., 38, L15708, https://doi.org/10.1029/2011GL048008.
- —, and Coauthors, 2015: The Community Earth System Model (CESM) large ensemble project: A community resource for studying climate change in the presence of internal climate variability. *Bull. Amer. Meteor. Soc.*, **96**, 1333–1349, https:// doi.org/10.1175/BAMS-D-13-00255.1.
- —, T. L'Ecuyer, H. Chepfer, N. Loeb, A. Morrison, and G. Cesana, 2016: Recent advances in Arctic cloud and climate research. *Curr. Climate Change Rep.*, 2, 159–169, https:// doi.org/10.1007/s40641-016-0051-9.
- Keen, A., and Coauthors, 2021: An inter-comparison of the mass budget of the Arctic sea ice in CMIP6 models. *Cryosphere*, **15**, 951–982, https://doi.org/10.5194/tc-15-951-2021.
- Labe, Z., G. Magnusdottir, and H. Stern, 2018: Variability of Arctic sea ice thickness using PIOMAS and the CESM large ensemble. J. Climate, 31, 3233–3247, https://doi.org/10.1175/ JCLI-D-17-0436.1.
- —, Y. Peings, and G. Magnusdottir, 2020: Warm Arctic, cold Siberia pattern: Role of full Arctic amplification versus sea ice loss alone. *Geophys. Res. Lett.*, 47, e2020GL088583, https://doi.org/10.1029/2020GL088583.
- Lehner, F., F. Joos, C. C. Raible, J. Mignot, A. Born, K. M. Keller, and T. F. Stocker, 2015: Climate and carbon cycle dynamics in a CESM simulation from 850 to 2100 CE. *Earth Syst. Dyn.*, 6, 411–434, https://doi.org/10.5194/esd-6-411-2015.
- Li, Z., Q. Ding, M. Steele, and A. Schweiger, 2022: Recent upper Arctic Ocean warming expedited by summertime atmospheric processes. *Nat. Commun.*, 13, 362, https://doi.org/10. 1038/s41467-022-28047-8.
- Lindsay, R., and J. Zhang, 2005: The thinning of Arctic sea ice, 1988–2003: Have we passed a tipping point? J. Climate, 18, 4879–4894, https://doi.org/10.1175/JCLI3587.1.
- —, M. Wensnahan, A. Schweiger, and J. Zhang, 2014: Evaluation of seven different atmospheric reanalysis products in the Arctic. J. Climate, 27, 2588–2606, https://doi.org/10.1175/JCLI-D-13-00014.1.
- Liu, J., M. Song, R. Horton, and Y. Hu, 2013: Reducing spread in climate model projections of a September ice-free Arctic. *Proc. Natl. Acad. Sci. USA.*, 110, 12571–12576, https://doi. org/10.1073/pnas.1219716110.
- Luo, R., Q. Ding, Z. Wu, I. Baxter, M. Bushuk, Y. Huang and X. Dong, 2021: Summertime atmosphere-sea ice coupling in

- the Arctic simulated by CMIP5/6 models: Importance of large-scale circulation. *Climate Dyn.*, **56**, 1467–1485, https://doi.org/10.1007/s00382-020-05543-5.
- McIlhattan, E. A., J. E. Kay, and T. S. L'Ecuyer, 2020: Arctic clouds and precipitation in the Community Earth System Model version 2. J. Geophys. Res. Atmos., 125, e2020JD032521, https://doi.org/10.1029/2020JD032521.
- Meehl, G. A., C. T. Chung, J. M. Arblaster, M. M. Holland, and C. M. Bitz, 2018: Tropical decadal variability and the rate of Arctic sea ice decrease. *Geophys. Res. Lett.*, 45, 11 326–11 333, https://doi.org/10.1029/2018GL079989.
- Middlemas, E. A., J. E. Kay, B. M. Medeiros, and E. A. Maroon, 2020: Quantifying the influence of cloud radiative feedbacks on Arctic surface warming using cloud locking in an Earth system model. *Geophys. Res. Lett.*, 47, e2020GL089207, https://doi.org/10.1029/2020GL089207.
- Mori, M., M. Watanabe, H. Shiogama, J. Inoue, and M. Kimoto, 2014: Robust Arctic sea-ice influence on the frequent Eurasian cold winters in past decades. *Nat. Geosci.*, 7, 869–873, https://doi.org/10.1038/ngeo2277.
- Morrison, A., J. E. Kay, W. Frey, H. Chepfer, and R. Guzman, 2019: Cloud response to Arctic sea ice loss and implications for future feedback in the CESM1 climate model. *J. Geophys. Res. Atmos.*, **124**, 1003–1020, https://doi.org/10.1029/ 2018JD029142.
- Msadek, R., G. A. Vecchi, M. Winton, and R. Gudgel, 2014: Importance of initial conditions in seasonal predictions of Arctic sea ice extent. *Geophys. Res. Lett.*, 41, 5208–5215, https://doi.org/10.1002/2014GL060799.
- Nakamura, T., K. Yamazaki, K. Iwamoto, M. Honda, Y. Miyoshi, Y. Ogawa, and J. Ukita, 2015: A negative phase shift of the winter AO/NAO due to the recent Arctic Sea-ice reduction in late autumn. J. Geophys. Res. Atmos., 120, 3209–3227, https://doi.org/10.1002/2014JD022848.
- Notz, D., and J. Marotzke, 2012: Observations reveal external driver for Arctic Sea-ice retreat. *Geophys. Res. Lett.*, 39, L08502, https://doi.org/10.1029/2012GL051094.
- —, and SIMIP Community, 2020: Arctic sea ice in CMIP6. Geophys. Res. Lett., 47, e2019GL086749, https://doi.org/10. 1029/2019GL086749.
- Ogi, M., Y. Tachibana, and K. Yamazaki, 2003: Impact of the wintertime North Atlantic Oscillation (NAO) on the summertime atmospheric circulation. *Geophys. Res. Lett.*, 30, 1704, https://doi.org/10.1029/2003GL017280.
- Olonscheck, D., T. Mauritsen, and D. Notz, 2019: Arctic sea-ice variability is primarily driven by atmospheric temperature fluctuations. *Nat. Geosci.*, 12, 430–434, https://doi.org/10.1038/ s41561-019-0363-1.
- Otto-Bliesner, B. L., and Coauthors, 2016: Climate variability and change since 850 CE: An ensemble approach with the Community Earth System Model. *Bull. Amer. Meteor. Soc.*, 97, 735–754, https://doi.org/10.1175/BAMS-D-14-00233.1.
- Overland, J. E., and M. Wang, 2013: When will the summer Arctic be nearly sea ice free? Geophys. Res. Lett., 40, 2097–2101, https://doi.org/10.1002/grl.50316.
- Papritz, L., 2020: Arctic lower-tropospheric warm and cold extremes: Horizontal and vertical transport, diabatic processes, and linkage to synoptic circulation features. *J. Climate*, 33, 993–1016, https://doi.org/10.1175/JCLI-D-19-0638.1.
- Perlwitz, J., M. Hoerling, and R. Dole, 2015: Arctic tropospheric warming: Causes and linkages to lower latitudes. *J. Climate*, 28, 2154–2167, https://doi.org/10.1175/JCLI-D-14-00095.1.

- Polyakov, I. V., and Coauthors, 2020: Weakening of cold halocline layer exposes sea ice to oceanic heat in the eastern Arctic Ocean. J. Climate, 33, 8107–8123, https://doi.org/10.1175/ JCLI-D-19-0976.1.
- Rampal, P., J. Weiss, C. Dubois, and J.-M. Campin, 2011: IPCC climate models do not capture Arctic sea ice drift acceleration: Consequences in terms of projected sea ice thinning and decline. J. Geophys. Res., 116, C00D07, https://doi.org/10.1029/2011JC007110.
- Roach, L. A., and E. Blanchard-Wrigglesworth, 2022: Observed winds crucial for September Arctic Sea ice loss. *Geophys. Res. Lett.*, 49, e2022GL097884, https://doi.org/10.1029/2022GL097884.
- Rosenblum, E., and I. Eisenman, 2016: Faster Arctic sea ice retreat in CMIP5 than in CMIP3 due to volcanoes. *J. Climate*, **29**, 9179–9188, https://doi.org/10.1175/JCLI-D-16-0391.1.
- Screen, J. A., and C. Deser, 2019: Pacific Ocean variability influences the time of emergence of a seasonally ice-free Arctic Ocean. *Geophys. Res. Lett.*, 46, 2222–2231, https://doi.org/10.1029/2018GL081393.
- Shepherd, T. G., 2014: Atmospheric circulation as a source of uncertainty in climate change projections. *Nat. Geosci.*, 7, 703–708, https://doi.org/10.1038/ngeo2253.
- Sigmond, M., J. C. Fyfe, and N. C. Swart, 2018: Ice-free Arctic projections under the Paris Agreement. *Nat. Climate Change*, 8, 404–408, https://doi.org/10.1038/s41558-018-0124-y.
- Simmonds, I., and I. Rudeva, 2012: The great Arctic cyclone of August 2012. Geophys. Res. Lett., 39, L23709, https://doi.org/ 10.1029/2012GL054259.
- Smedsrud, L. H., M. H. Halvorsen, J. C. Stroeve, R. Zhang, and K. Kloster, 2017: Fram Strait sea ice export variability and September Arctic sea ice extent over the last 80 years. *Cryosphere*, 11, 65–79, https://doi.org/10.5194/tc-11-65-2017.
- Smirnova, J., and P. Golubkin, 2017: Comparing polar lows in atmospheric reanalyses: Arctic system reanalysis versus ERA-Interim. *Mon. Wea. Rev.*, 145, 2375–2383, https://doi.org/10.1175/MWR-D-16-0333.1.
- Smith, A., and A. Jahn, 2019: Definition differences and internal variability affect the simulated Arctic sea ice melt season. *Cryosphere*, **13**, 1–20, https://doi.org/10.5194/tc-13-1-2019.
- Sotiropoulou, G., J. Sedlar, R. Forbes, and M. Tjernström, 2016: Summer Arctic clouds in the ECMWF forecast model: An evaluation of cloud parametrization schemes. *Quart. J. Roy. Meteor. Soc.*, **142**, 387–400, https://doi.org/10.1002/qj.2658.
- Spreen, G., L. de Steur, D. Divine, S. Gerland, E. Hansen, and R. Kwok, 2020: Arctic sea ice volume export through Fram Strait from 1992 to 2014. J. Geophys. Res. Oceans, 125, e2019JC016039, https://doi.org/10.1029/2019JC016039.
- Steiger, N. J., J. E. Smerdon, E. R. Cook, and B. I. Cook, 2018: A reconstruction of global hydroclimate and dynamical variables over the Common Era. Sci. Data, 5, 180086, https://doi. org/10.1038/sdata.2018.86.
- Stroeve, J. C., M. M. Holland, W. Meier, T. Scambos, and M. Serreze, 2007: Arctic sea ice decline: Faster than forecast. *Geophys. Res. Lett.*, 34, L09501, https://doi.org/10.1029/2007GL029703.
- —, V. Kattsov, A. Barrett, M. Serreze, T. Pavlova, M. Holland, and W. N. Meier, 2012: Trends in Arctic sea ice extent from CMIP5, CMIP3 and observations. *Geophys. Res. Lett.*, 39, L16502, https://doi.org/10.1029/2012GL052676.
- —, T. Markus, L. Boisvert, J. Miller, and A. Barrett, 2014: Changes in Arctic melt season and implication for sea ice loss. *Geophys. Res. Lett.*, 41, 1216–1225, https://doi.org/10. 1002/2013GL058951.

- Swart, N. C., J. C. Fyfe, E. Hawkins, J. E. Kay, and A. Jahn, 2015: Influence of internal variability on Arctic sea-ice trends. *Nat. Climate Change*, 5, 86–89, https://doi.org/10.1038/nclimate2483.
- Tan, I., and T. Storelvmo, 2019: Evidence of strong contributions from mixed-phase clouds to Arctic climate change. *Geophys. Res. Lett.*, 46, 2894–2902, https://doi.org/10.1029/2018GL081871.
- Tardif, R., and Coauthors, 2019: Last millennium reanalysis with an expanded proxy database and seasonal proxy modeling. Climate Past, 15, 1251–1273, https://doi.org/10.5194/cp-15-1251-2019.
- Taylor, K. E., M. Crucifix, P. Braconnot, C. D. Hewitt, C. Doutriaux, A. J. Broccoli J. F. B. Mitchell, and M. J. Webb, 2007: Estimating shortwave radiative forcing and response in climate models. *J. Climate*, 20, 2530–2543, https://doi.org/10.1175/JCLI4143.1.
- Thorndike, A. S., and R. Colony, 1982: Sea ice motion in response to geostrophic winds. J. Geophys. Res., 87, 5845–5852, https:// doi.org/10.1029/JC087iC08p05845.
- Tietsche, S., D. Notz, J. H. Jungelaus, and J. Marotzke, 2011: Recovery mechanisms of Arctic summer sea ice. *Geophys. Res. Lett.*, 38, L02707, https://doi.org/10.1029/2010GL045698.
- Topál, D., Q. Ding, J. Mitchell, I. Baxter, M. Herein, T. Haszpra, R., Luo, and Q. Li, 2020: An internal atmospheric process determining summertime Arctic sea ice melting in the next three decades: Lessons learned from five large ensembles and multiple CMIP5 climate simulations. *J. Climate*, 33, 7431– 7454, https://doi.org/10.1175/JCLI-D-19-0803.1.
- Wang, B., X. Zhou, Q. Ding, and J. Liu, 2021: Increasing confidence in projecting the Arctic ice-free year with emergent constraints. *Environ. Res. Lett.*, 16, 094016, https://doi.org/10.1088/1748-9326/ac0b17.
- Wang, C., R. M. Graham, K. Wang, S. Gerland, and M. A. Granskog, 2019: Comparison of ERA5 and ERA-Interim near-surface air temperature, snowfall and precipitation over Arctic sea ice: Effects on sea ice thermodynamics and evolution. *Cryosphere*, 13, 1661–1679, https://doi.org/10.5194/tc-13-1661-2019.
- Wang, W., M. Chen, and A. Kumar, 2013: Seasonal prediction of Arctic sea ice extent from a coupled dynamical forecast system. *Mon. Wea. Rev.*, **141**, 1375–1394, https://doi.org/10.1175/ MWR-D-12-00057.1.
- Wernli, H., and L. Papritz, 2018: Role of polar anticyclones and mid-latitude cyclones for Arctic summertime sea-ice melting. *Nat. Geosci.*, 11, 108–113, https://doi.org/10.1038/s41561-017-0041-0.
- Wettstein, J. J., and C. Deser, 2014: Internal variability in projections of twenty-first-century Arctic sea ice loss: Role of the large-scale atmospheric circulation. *J. Climate*, 27, 527–550, https://doi.org/10.1175/JCLI-D-12-00839.1.
- Winton, M., 2011: Do climate models underestimate the sensitivity of Northern Hemisphere sea ice cover? *J. Climate*, **24**, 3924–3934, https://doi.org/10.1175/2011JCLI4146.1.
- Yamagami, A., M. Matsueda, and H. L. Tanaka, 2017: Extreme Arctic cyclone in August 2016. Atmos. Sci. Lett., 18, 307–314, https://doi.org/10.1002/asl.757.
- Yang, W., G. A. Vecchi, S. Fueglistaler, L. W. Horowitz, D. J. Luet, Á. G. Muñoz, D. Paynter, and S. Underwood, 2019: Climate impacts from large volcanic eruptions in a high-resolution climate model: The importance of forcing structure. *Geophys. Res. Lett.*, 46, 7690–7699, https://doi.org/10.1029/2019GL082367.
- Zhang, R., 2015: Mechanisms for low-frequency variability of summer Arctic sea ice extent. *Proc. Natl. Acad. Sci. USA*, 112, 4570–4575, https://doi.org/10.1073/pnas.1422296112.